Experimental study on shear deformation of reinforced concrete beams using Digital Image Correlation

Zheng Huang[1], Yongming Tu[2], Shaoping Meng[3], Cristian Sabau[4], Cosmin Popescu[5], Gabriel Sas[6]

[1]Ph.D. Candidate, School of Civil Engineering, Southeast University, 210096, Nanjing, China. E-mail: zheng.huang.china@hotmail.com

[2]Associate Professor, School of Civil Engineering, Southeast University, 210096, Nanjing, China (corresponding author). E-mail: yongming.tu@ltu.se

[3]Professor, School of Civil Engineering, Southeast University, 210096, Nanjing, China. E-mail: mengshaoping@seu.edu.cn

[4]Ph.D. Candidate, Division of Structural Engineering, Luleå University of Technology, SE-971 87, Luleå, Sweden. E-mail: cristian.sabau@ltu.se

[5]Associate Senior Lecturer, Division of Structural Engineering, Luleå University of Technology, SE-971 87, Luleå, Sweden. E-mail: cosmin.popescu@ltu.se

[6]Research Scientist, Infrastructure, Materials and Structures, Norut, Narvik, N-8504, Narvik, Norway. E-mail: gabriel.sas@norut.no

Abstract: This paper presents an experimental program aimed at providing reliable and comprehensive experimental data for assessing the available models of predicting the shear deformation of diagonally-cracked reinforced concrete (RC) beams. The non-contact measuring technique, Digital Image Correlation (DIC), was used to monitor the full-field displacement and strain in the shear span of five RC beams with thin webs. Virtual measuring grids were created to measure the mean shear strain and other critical deformation results which reflects the mechanism of shear deformation after shear cracking (i.e. the principal compressive strain angle, the principal compressive strain, the mid-depth longitudinal strain and the mean vertical strain). The experimental mean shear strain and other critical deformation results were compared with the predictions with several available models. The comparison indicates the available models fail to reproduce the principal compressive strain angle, the mid-depth longitudinal strain and the mean vertical strain which constitute the key parameters in estimating the shear deformation after shear cracking. As a result, significant discrepancies in the shear deformation of the beams tested in this paper are observed between the experimental and calculated results. It is also found that the predicted shear deformation of a number of beam specimens tested by other researchers with the available models deviates considerably from the experimental results. In general, the existing models are not capable of providing accurate predictions of the shear deformation of RC beams and further investigation into this topic is needed.

Keywords: Reinforced concrete beams; shear deformation; experimental study; Digital Image Correlation

1. Introduction

Design and analysis for serviceability is one of the central parts of the design process for concrete structures. In the conventional design of reinforced concrete (RC) beams, the deflection due to shear is assumed to be relatively small compared to that due to flexure. Except for JSCE Guidelines for Concrete 2007 [1], the current codes of concrete structures, e.g. ACI318-14 [2], AASHTO [3], Model Code 2010 [4] and Eurocode 1992 [5], only provide methods for estimating flexure deformation. Some reported investigations into the existing concrete bridges around the world [6-9] have shown that diagonal cracks may appear in the web of the box girders during the service life. Moreover, the increased use of high-strength materials in concrete structures, coupled with more precise computer-aided design, has resulted in lighter and more material-efficient structural members [10], e.g. box girders with thin webs. Such design increases the risk of the shear cracking. Previous finite element (FE) analyses performed by Huang et al. [11] indicated that regarding the RC beams without shear reinforcement, the deformation of the shear span in the serviceability limit state was governed by flexure because failure occurred soon after the formation of diagonal cracks. However, in terms of the beams with shear reinforcement, the shear-induced deflection may not be negligible after shear cracking. In this context, neglecting the shear-induced deflection in the analysis of RC beams with stirrups could lead to un-conservative design. The focus of this paper is on the shear deformation of RC beams with shear reinforcement.

The number of the existing tests in which the shear deformation was directly measured is limited. Ueda et al. [12] measured the shear deformation in the shear span of four rectangular beams using the laser speckle method. According to Huang et al. [11], the method of calculating the experimental shear-induced deflection used by Ueda et al. [12], in which the shear span was divided into only one grid, could result in an overestimate of the actual shear-induced deflection. Hansapinyo et al. [13] reported an experimental program of four rectangular RC beams. Four measuring grids, each of which was composed of five traditional displacement transducers, were attached to the surface of the test beams. The shear-induced and flexure-induced deflections were experimentally obtained by integrating the corresponding deformation (i.e. the mean shear strain and the curvature) of all grids. Hansapinyo et al. [13] also compared the test results of shear-induced deflection obtained by two methods: (1) directly integrating the mean shear strain; and (2) subtracting the flexure-induced deflection from the total deflection. The comparison showed a notable discrepancy between the results obtained by the aforementioned two methods. The inconsistency was believed to be attributed to the cracks passing through the fixing points of the gauges which affected the measurements. Debernardi and Taliano [14] tested six RC beams with thin webs. Measuring grids composed of traditional sensors, which were similar with those adopted by Hansapinyo et al. [13], were applied to measure the curvature and the mean shear strain at different sections in the shear span. However, as the measuring grids were arranged at discrete locations, the shear-induced deflections were not directly measured in the tests. He et al. [15] and Zheng et al. [16] tested two restrained I-beams with thin webs and the mean shear strain near the point of contraflexure was measured using the traditional sensors. Several prestressed and nonprestressed beams were tested by various researchers at the University of Toronto [17]. These beams failed primarily due to the action of high shear stresses and the mean shear strain at the point of contraflexure was measured in the tests. An experimental study of the time-dependent shear deformation of strengthened and un-strengthened RC beams has been performed by Jin [18].

The available prediction models for the shear deformation of RC beams after shear cracking could be classified into three categories: (1) theoretical models based on the truss analogy [1, 12, 15, 19, 20]; (2) theoretical models based on the Modified Compression Field Theory (MCFT) [14, 21]; (3) empirical models based on the regression analysis [13, 22]. In terms of the models based on the truss analogy or the MCFT, the mean shear strain of one particular section after shear cracking was calculated assuming diagonal concrete struts between diagonal cracks acting as the compression struts while the stirrups as the tension ties. In the empirical models developed by Hansapinyo et al. [13] and Rahal [22], the tangent shear stiffness after shear cracking was obtained by the regression analysis of the numerical or experimental results. The detailed information of these models is presented in Section 2. As can be seen in Section 2, with regard to the models based on either the truss analogy or the MCFT, the inclination of the diagonal compression struts (or the principal compressive strain angle if they are assumed to be consistent), θ, the principal compressive strain, ε_2, and the mean vertical strain, ε_y, (or the mid-depth longitudinal strain, ε_x) suggest the mechanism of the shear deformation of RC beams after shear cracking. These deformation results also constitute the critical parameters in estimating the mean shear strain. However, none of the existing tests reported the measurements of all these critical parameters. Accordingly, further experimental investigation into the shear deformation of RC beams, in which not only the mean shear strain, but also the principal compressive strain angle, the principal compressive strain, the mean vertical strain and the mid-depth longitudinal strain at various sections are carefully measured, could be helpful in assessing the available models.

Because cracks on the concrete surface could influence the measurement of the deformation if the measuring grids are composed of traditional sensors as discussed above, non-contact optical measuring approach is expected to be an alternative to overcome this drawback. Digital Image Correlation (DIC) is a full-field measuring approach and has become a reliable method for measuring the surface displacement and strain in the test of concrete structures [23-26]. In this paper, the DIC technique is used to investigate the shear deformation of five RC beams with thin webs. The superiority of this non-contact optical measuring approach over traditional sensors in monitoring the deformation results of concrete structures is demonstrated. Also, the mean shear strain, γ, along with the critical parameters in predicting the shear deformation (i.e. θ, ε_2, ε_y and ε_x) is carefully measured. The deformation results obtained from this experimental program along with others collected from the literature are compared with the predictions with the available models. This study is intended to provide reliable experimental evidences for assessing the related prediction models and also, for future studies on the shear deformation of RC beams.

2. Available prediction models

Six available prediction models for estimating the shear deformation are reviewed in this section. These models include: (1) JSCE Model proposed by JSCE [1]; (2) Ueda Model proposed by Ueda et al. [12]; (3) He Model proposed by He et al. [15]; (4) Deb Model proposed by Debernardi et al. [21]; (5) Han Model proposed by Hansapinyo et al. [13]; and (6) Rahal Model proposed by Rahal [22].

2.1. JSCE Model and Ueda Model

In these two models, the estimation of shear deformation after cracking included two stages: (1) after flexure cracking and before shear cracking; and (2) after shear cracking.

At Stage 1, the expressions given by these two models were the same. The reduced shear stiffness of the section due to flexure cracking was calculated by introducing the effective section area, A_e. The equations for the shear deformation are shown below:

$$\gamma = \frac{k_v V}{G_c A_e} \tag{1}$$

$$A_e = A_g \cdot \left(\frac{M_{cr}}{M_{\max}}\right)^3 + A_{cr} \cdot \left[1 - \left(\frac{M_{cr}}{M_{\max}}\right)^3\right] \le A_g \tag{2}$$

where γ is the shear strain; k_v is the shear coefficient depending on the shape of the cross section (1.2 for rectangular cross section); V is the external shear force; G_c is the shear modulus of elasticity of concrete; M_{cr} is the flexural cracking moment; M_{max} is the maximum moment applied to the beam; A_g is the area of the gross section; and A_{cr} is the area of the cracked section.

At Stage 2, i.e. after shear cracking (whether or not flexure cracking has occurred), the expressions for estimating the shear deformation given by these two models were based on the truss analogy. The shear strain was considered to be induced by the shortening of the diagonal compression struts, ε_2, and the elongation of the vertical tension ties (i.e. the mean vertical strain), ε_y. The expressions are shown:

$$\gamma = \frac{\varepsilon_y}{\cot\theta} - \frac{\varepsilon_2}{\sin\theta \cdot \cos\theta} \tag{3}$$

where θ is the angle between the diagonal concrete struts and the longitudinal axis of the beam. JSCE Model and Ueda Model provided two different expressions for θ. In JSCE Model, the inclination of diagonal concrete struts (degree) was calculated as:

$$\theta = 45 - \left(3.2 - 7800 \cdot \rho_{st} \cdot \rho_{sw}\right) \cdot \left(a/d\right) \cdot \frac{V - V_{cr}}{b_w \cdot d} \tag{4}$$

where ρ_{st} is the tension reinforcement ratio; ρ_{sw} is the shear reinforcement ratio; a is the shear span; d is the effective depth; V_{cr} is the shear cracking load; and b_w is the web width. The expression for θ (degree) used in Ueda Model is as follows:

$$\begin{cases} \theta = -\left(0.4\cdot\left(\dfrac{a}{d}\right)^2 + 2.9\right)\left(\dfrac{V - V_{cr}}{b_w d}\right)^2 + 3.2\cdot\left(\dfrac{a}{d}\right) + 40.2 & V_{cr} \le V < 1.7\cdot V_{cr} \\ \theta = \theta_1 \cdot \left(\dfrac{1.7\cdot V_{cr}}{V}\right)^{\left(0.7 - 32\cdot\sqrt{\rho_{st}\cdot\rho_{sw}}\right)\cdot\frac{a}{d}} & V \ge 1.7\cdot V_{cr} \end{cases} \tag{5}$$

$$\theta_1 = -\left(0.4\cdot\left(\frac{a}{d}\right)^2 + 2.9\right)\left(\frac{1.7\cdot V_{cr} - V_{cr}}{b_w d}\right)^2 + 3.2\cdot\left(\frac{a}{d}\right) + 40.2 \tag{6}$$

After shear cracking, the stiffness of the tension ties was assumed to be composed of two parts: (1) the shear reinforcement; and (2) the effective concrete surrounding the stirrups. Thus, the elongation of the tension ties, ε_y, was determined as:

$$\varepsilon_y = \frac{\left(V - V_{cr}\right)\cdot s_w}{\left(E_{sw}\cdot A_{sw} + E_c\cdot A_{ce}\right)\cdot 0.9\cdot d\cdot\cot\theta} \tag{7}$$

$$A_{ce} = A_{ceo}\cdot\left(V_{cr}/V\right)^3 \tag{8}$$

$$A_{ceo} = \min\left(\sqrt{\frac{A_{sw}\cdot f_{ysw}}{f_t}}, s_w\right)\cdot b_w \le \frac{A_{sw}\cdot f_{ysw}}{f_t} \tag{9}$$

where s_w is the spacing of the stirrups; E_{sw} is the elastic modulus of the stirrups; A_{sw} is the area of the stirrups; E_c is the elastic modulus of the concrete; A_{ce} is the area of the effective concrete surrounding the stirrups at the shear force level of V; A_{ceo} is the area of the effective concrete surrounding the stirrups at the shear force level of V_{cr}; f_{ysw} is the yield stress of the stirrups; and f_t is the tensile strength of the concrete.

The diagonal concrete struts were assumed to be elastic after shear cracking and its deformation, ε_2, was determined as:

$$\varepsilon_2 = -\frac{V - V_{cr}}{E_c \cdot b_w \cdot 0.9 \cdot d \cdot \sin\theta \cdot \cos\theta} \tag{10}$$

2.2. He Model

He et al. [15] proposed an explicit equation for estimating the secant shear stiffness of fully diagonally cracked section when the stirrups yielded, K_y. The derivation of K_y was based on the truss analogy. The simplified expression of K_y obtained through the least-square fitting is as follows:

$$K_y = \sqrt[3]{\rho_{sw}} \cdot K_e \tag{11}$$

where K_e is the elastic shear stiffness which could be taken as $G_c \cdot b_w \cdot 0.9 \cdot d$。

With respect to the stage between the shear cracking and the stirrups yielding, the secant shear stiffness, K_s, was calculated as the cubic polynomial interpolation between K_e and K_y, i.e.:

$$\begin{cases} K_s = \dfrac{\left(1-\sqrt[3]{\rho_{sw}}\right)\cdot\left(-8\cdot\lambda_V^3 + 16\cdot\lambda_V^2 - 11\cdot\lambda_V\right)+3}{3}\cdot K_e \\ \lambda_V = \dfrac{V - V_{cr}}{V_y - V_{cr}} \end{cases} \tag{12}$$

where V_y is the shear force when the stirrups yield. He et al. [15] suggested the following equation for estimating V_y in the absence of more sophisticated expressions:

$$V_y = 0.17 \cdot \sqrt{f_c} \cdot b_w \cdot d + \rho_{sw} \cdot f_{ysw} \cdot b_w \cdot 0.9 \cdot d \cdot \cot 45° \tag{13}$$

2.3. Deb Model

Debernardi and Taliano [14] proposed a model (termed Mixed Model) based on the MCFT for determining the shear deformation of the sections in the Bernoulli region.

The Bernoulli region, also referred to as the B-region, refers to the area in which the hypothesis of plane-section is assumed valid. By contrast, the strain distribution in the disturbance region (referred to as the D-region) is significantly nonlinear [27]. Additionally, Debernardi et al. [21] derived a simplified model based on the Mixed Model. In this paper, the simplified model is termed Deb Model and will be presented in detail.

In Deb Model, the shear strain of the section in the B-region was calculated according to the Mohr circle：

$$\gamma = \frac{2 \cdot (\varepsilon_x - \varepsilon_2)}{\tan\theta} \tag{14}$$

where ε_x is the mid-depth longitudinal strain.

It was observed in the experiments [14] that after shear cracking, the shear force increased the amount of the tension strain in the bottom flange, ε_{bot}, and decreased the amount of the compression strain, ε_{top}, in the top flange. The corresponding equations are as follows:

$$\begin{aligned} \varepsilon_{top} &= \left[M + \frac{(V - V_{cr})}{2} \cdot 0.9 \cdot d \cdot \cot\theta \right] \cdot \frac{d - x_c}{E_c \cdot I_e} \\ \varepsilon_{bot} &= \left[-M + \frac{(V - V_{cr})}{2} \cdot 0.9 \cdot d \cdot \cot\theta \right] \cdot \frac{x_c - 0.1 \cdot d}{E_c \cdot I_e} \end{aligned} \tag{15}$$

where M is the external moment; x_c is the compression depth of the cross section; and I_e is the effective moment of inertia of the cross section, which could be estimated according to either ACI318-14 [2] or Eurocode [5]. Then, the mid-depth longitudinal strain is calculated as the average of ε_{bot} and ε_{top}:

$$\varepsilon_x = \frac{\varepsilon_{top} + \varepsilon_{bot}}{2} \tag{16}$$

The expression for estimating ε_2 in Deb Model is similar to that in JSCE Model and Ueda Model but with a slight difference:

$$\varepsilon_2 = -\frac{V - V_{cr} \cdot \sin^2\theta}{E_c \cdot b_w \cdot 0.9 \cdot d \cdot \sin\theta \cdot \cos\theta} \tag{17}$$

The inclination of the diagonal compression struts, which was assumed to be consistent with the principal compression strain angle, was found to be dependent on the following four major factors: (1) the mid-depth longitudinal strain, ε_x; (2) the external shear force, V; (3) the shear reinforcement ratio, ρ_{sw}; and (4) the characteristic value of the concrete compressive strength, f_{ck}. The equation for θ is as follows:

$$\begin{cases} \theta = c_1 \cdot \left(\dfrac{V - V_{cr}}{b_w \cdot d \cdot f_t} \right)^{c_2} \cdot c_3 \cdot c_4 \\ c_1 = 30 + \rho_{sw} \cdot 1150 \\ c_2 = 5 \cdot \rho_{sw} - 0.215 \\ c_3 = 1 + 0.1 \cdot \left(\dfrac{f_{ck} - 25}{25} \right) \\ c_4 = 0.64 + 960 \cdot \varepsilon_x - 6 \times 10^5 \cdot \varepsilon_x^2 \end{cases} \tag{18}$$

2.4. Han Model

Hansapinyo et al. [13] proposed an empirical model for estimating the reduced tangent shear modulus, G_{cr}, of RC shear panels under uniform loads after shear cracking. The ratio of G_{cr} to the elastic shear modulus was found to be dependent on the longitudinal strain and the stirrup ratio:

$$\frac{G_{cr}}{G_c} = -68400 \cdot \varepsilon_l^2 - 130 \cdot \varepsilon_l + \left(140 - \frac{139.79}{\rho_{sw}^{0.00028}} \right) \tag{19}$$

where ε_l is the longitudinal strain.

With the aim of determining the tangent shear stiffness of one particular section of RC beams, the cross section was first divided into several layers and the variance of the longitudinal strain induced by the moment could thus be estimated. After the flexure cracking occurred (before shear cracking), the tangent shear modulus of the layer in compression was assumed to be elastic while that of the layer in tension was calculated according to **Eq. (19)**. After shear cracking, the tangent shear modulus of all layers was considered to be degraded and was determined with **Eq. (19)**.

2.5. Rahal Model

Based on the experimental results of 40 RC shear panels, Rahal [22] developed an empirical model for estimating the post-shear-cracking tangent shear modulus of the members subjected to pure shear. The proposed model was validated against the zone of the negligible bending moment in one RC beam with symmetrical longitudinal reinforcement [22]. The post-shear-cracking tangent shear modulus, G_{cr}, was influenced by the following three parameters: (1) the concrete compressive strength; (2) the amount of the orthogonal reinforcement; and (3) the strength of the orthogonal reinforcement. The equations are shown below:

$$G_{cr} = 135 \cdot f_c \cdot \sqrt{w_{sx} \cdot w_{sy}} \tag{20}$$

$$\begin{cases} w_{sx} = \dfrac{\rho_{sx} f_{ysx}}{f_c} \le \dfrac{1}{3} - \dfrac{f_c}{900} \\ w_{sy} = \dfrac{\rho_{sy} f_{ysy}}{f_c} \le \dfrac{1}{3} - \dfrac{f_c}{900} \end{cases} \tag{21}$$

where G_{cr} and f_c are in MPa; ρ_{sx} and ρ_{sy} are the ratios of the orthogonal reinforcement; and f_{ysx} and f_{ysy} are the yield strength of the orthogonal reinforcement (MPa).

3. Experimental program

3.1. Specimens

Five RC beams with thin webs were tested in this experimental program. All of them had the same cross section with a height of 600 mm. The span and the shear span was 5000 mm and 2250 mm, respectively. The shear span-to-effective depth ratio was approximately 4:1. All the beam specimens were symmetrically reinforced with stirrups in the two shear spans. The test variables included the stirrup ratio, the stirrup spacing, the tension reinforcement ratio and the web width. The details of the beam specimens are summarized in **Table 1** and **Fig. 1**.

All the beam specimens were cast with ready-mix concrete transported by one truck from a local concrete plant. After casting, the specimens were kept moist with wet burlap for 7 days and then exposed to air dry in the laboratory until the day of testing. The age of concrete at the time of testing was around 30 days. To determine the mechanical properties of concrete, nine 150×300 mm concrete cylinders were cast from the same truck and cured under the same conditions as the beam specimens. The mean cylinder compressive strength f_c was 40 MPa (COV 6.2%) and the average modulus of elasticity E_c was 34 GPa (COV 5.3%). Deformed steel re-bars of Chinese standard HRB400 were used as the longitudinal reinforcements and the stirrups. The mechanical properties of the steel re-bars were tested and the results are listed in **Table 2**.

3.2. Test setup and instrumentation

The general view of the test setup and the instrumentation is shown in **Fig. 2**.

The beam specimens were simply supported. The load was first applied to a steel beam through a servo-hydraulic jack with an ultimate load of 1000 kN and then transferred to the beam specimen. The pure-bending length of the beams was only 500 mm as the pure bending was not the focus of this paper. All beams were tested to failure with a loading rate of 0.02 mm/s.

PMLAB, which was co-developed by the Optical Mechanics Groups at Southeast University (SEU) and University of Science and Technology of China (USTC), was used as the 3D-DIC measuring technique in this program. The full-field displacement and strain of the two shear spans of the beams were simultaneously measured by four camera systems, each of which consisted of two industrial cameras (see **Fig. 1**(a) and **Fig. 2**). The measuring zone of each system was approximately 600 mm × 1200 mm. The targets were evenly spaced 112.5 mm apart on the top and bottom flanges of the beam as shown in **Fig. 1**. The displacements of these targets were tracked by the 3D-DIC technique and used to create the virtual measuring grids (VGs) for evaluating the deformation of the grids (see Section 3.3 for details). Random speckle patterns were required aimed at the full-field strain measurement. Owing to the large area monitored, water transfer printing method [28] was applied for the sake of efficiency (see **Fig. 2**(b)). In this method, pieces of transfer papers made of prefabricated decal papers, protected sheets and printed speckle patterns were required. Before testing, the speckle patterns were generated by computer simulations, printed on the decal paper and then transferred to one surface of the two shear spans of the beams by moistening the basement with water using a brush (However, in terms of specimen S1, the speckle pattern was only applied to the right shear span and hence, the full-field strain results were recorded only in the right shear span). The crack patterns in the measured zones, represented by the principal tensile strain, were obtained by the 3D-DIC technique. The loading procedure was paused every 10 kN to acquire the images from all the four camera systems.

3.3. Virtual measuring grids (VGs)

The schematic diagram of the arrangement of virtual measuring grids is shown in **Fig. 3**(a). As the area near the loading point was hidden by the column of the loading setup, the measuring length of one shear span of all specimens was finally 2025 mm rather than the shear span of 2250 mm. The monitored area was divided into four parts, i.e. four virtual measuring grids, which were termed from VG1 to VG4 sequentially from the loading point to the support (see **Fig. 3**(a)). VG1 and VG3 measured 560 × 450 mm while VG2 and VG4 560 × 562.5 mm. The moment-to-shear ratio of the virtual measuring grid, which is denoted by a_g, could be taken as the distance between the support and the centre of the grid. The corresponding values of a_g for VG1 to VG4 were 1800 mm, 1294 mm, 788 mm and 281 mm, respectively.

A virtual measuring grid was composed of 4 corner targets (TG1 through TG4) and a number of intermediate targets on the top and bottom flanges, as shown in **Fig. 3**(b). The numbers of the intermediate targets were 8 for the grids with the length of 562.5 mm and 6 for those with the length of 450 mm. The longitudinal and vertical displacements of the corner targets are denoted as u_i and v_i (i represents the label of the target), respectively. The height and the length of a grid are denoted as l_g and h_g.

The mid-depth longitudinal strain of a grid, ε_x, was calculated as:

$$\varepsilon_x = \frac{\varepsilon_{top} + \varepsilon_{bot}}{2} \tag{22}$$

where ε_{top} is the longitudinal strain of the top flange of a grid, equal to $(u_4\text{-}u_1)/l_g$; and ε_{bot} is the longitudinal strain of the bottom flange of a grid, equal to $(u_3\text{-}u_2)/l_g$.

In the experimental program conducted by Debernardi and Taliano [14], the mean vertical strain of a grid was calculated as the average of the vertical strain of the left and right edges, i.e.:

$$\varepsilon_y = \frac{(v_1 - v_2) + (v_4 - v_3)}{2 \cdot h_g} \tag{23}$$

Fig. 4 presents the variance of the experimentally obtained mean vertical strain in the right shear span of specimen S1 at the shear force level of 150 kN. The vertical strain of one particular cross section was estimated by $(v_{top}-v_{bot})/h_g$, where v_{top} and v_{bot} are the vertical displacements of the targets at the top and bottom flanges, respectively. **Fig. 4** indicates significant fluctuations of the vertical strain along the beam axis. The circles in **Fig. 4** mark the vertical strain at the edges of VG2 and VG3. It could be found that the vertical strain at the intermediate sections between the two edges were larger than the average of the vertical strain of the left and right edges. The reason could be identified in **Fig. 5**, which shows the crack pattern in the right shear span of specimen S1 at the same shear force level. The dash lines in **Fig. 5** represent the intermediate cross sections. The crack pattern indicated more (or wider) diagonal cracks in some of the intermediate cross sections which resulted in the corresponding larger vertical strain. Consequently, the actual mean vertical strain would be underestimated by simply averaging the results of the left and right edges. Regarding another virtual measuring grid, for which section A and section B (see **Fig. 4**) were selected as the left and right edges, the actual mean vertical strain would be overestimated instead if following the method presented by Debernardi and Taliano [14]. This method shows a lack of objectivity. Hence, in this paper, the mean vertical strain of a grid was calculated by averaging the measured vertical strain of all sections inside the grid.

The mean shear strain of a grid was calculated with the method presented by Huang et al. [11]. The expression is shown below:

$$\gamma = \frac{u_1 + u_4 - u_2 - u_3}{2 \cdot h_g} + \frac{v_3 + v_4 - v_1 - v_2}{2 \cdot l_g} \tag{24}$$

The principal tensile strain ε_1, the principal compressive strain ε_2 and the principal compressive strain angle θ could thus be estimated by the three strain components (i.e. ε_x, ε_y and γ) based on the Mohr circle. Additionally, the curvature of a grid was calculated as:

$$\kappa = \frac{\varepsilon_{bot} - \varepsilon_{top}}{h_g} \tag{25}$$

The shear-induced deflection of the measuring area in one shear span was obtained by integrating the shear strain along the shear span:

$$\delta_s = \sum_{i=1}^{4} \gamma_{xy}^i \cdot l_g^i \tag{26}$$

The flexure-induced deflection was calculated by a set of recursion formulas, which was presented by Huang et al. [11]. The expressions are shown below:

$$\begin{gathered} \delta_f^i = \delta_f^{i-1} + \alpha^i \cdot l_g + \frac{1}{2} \cdot \kappa^i \cdot l_g^2 \\ \alpha^i = \alpha^{i-1} + \alpha_g^{i-1} \\ \delta_f^0 = 0 \\ \alpha^0 = \alpha_{bearing} \\ \alpha_g^0 = 0 \end{gathered} \tag{27}$$

where δ_f^i is the flexure-induced deflection at the right-most of the i^{th} grid as shown in **Fig. 3**; α^i is the rotation angle of the left edge of the i^{th} grid; α_g^i is the mean rotation angle within the grid, which is taken as $\kappa \cdot l_g$; and $\alpha_{support}$ is the rotation angle at the support and could be calculated:

$$\alpha_{support} = \frac{u_{top,support} - u_{bot,support}}{h_g} \tag{28}$$

where $u_{top,support}$ and $u_{bot,support}$ are the longitudinal displacements of the targets at the top and bottom flange of the support cross section, respectively.

4. Experimental results

4.1. General behaviour

Extensive diagonal cracks in the shear spans were observed for all specimens as the load level increased. All beams presented a typical flexure failure characterized by the yielding of the tension reinforcement and the concrete crush at the top of the mid-span cross section (see **Fig. 6**). The peak shear forces were 157.5 kN for S4 and around 260 kN for the other specimens.

During the test of specimen S2 only the right shear span were successfully measured by the 3D-DIC technique because of the failure of several camera systems. Only the measurements in the left shear span were obtained for specimen S5 due to similar reasons. After striping the forms of specimen S4, several relatively large voids were observed on the top surface of the bottom flange in the right shear span and the tension reinforcement was partly exposed. The phenomenon was believed to be attributed to the inadequate vibration when casting the beam. Although fresh concrete had been placed to fill the voids, owing to the potential poor bond performance between the tension reinforcement and the new concrete, unexpected longitudinal cracks were observed in the right shear span during the test (see **Fig. 7**). This led to extremely large deformation in the right shear span of S4 compared with that in the left shear span. Thus, the experimental results of the right shear span of specimen S4 are omitted in this paper.

4.2. Cracking loads

The experimentally observed flexural and shear cracking loads are summarized in

Table 3.

Fig. 8 illustrates the crack patterns of the left and right shear spans of specimen S3 at the shear cracking loads of different measuring grids. As the load level rose, the cracks appeared sequentially from the loading point to the support.

The flexural cracking moment, M_{cr}, could be calculated with the elastic beam theory:

$$M_{cr} = \frac{f_t \cdot I_g}{y_t} \tag{29}$$

where I_g is the moment of inertia of the gross section; and y_t is the distance between the centroid and the extreme tension fibre. The concrete tensile strength, f_t, could be calculated in accordance with Model Code 2010 [4] based on the measured concrete compressive strength. The calculated results of the mean value, the lower bound value and the upper bound value of f_t are 3.0 MPa, 2.1 MPa and 3.9 MPa, respectively. Through fitting the experimental results of the flexure cracking loads, 3.6 MPa is selected for f_t. The calculated flexural cracking loads match the experimental results for all specimens except for S4 as shown in **Fig. 9**. The lower flexural cracking loads of specimen S4 might be attributed to the unexpected concrete shrinkage. As recommended by Kaklauskas et al. [29], the shrinkage could be modelled by a fictitious axial force applied to an un-symmetrical section (as the cross section of the beams in this paper was un-symmetrically longitudinally reinforced). The reader is referred to Kaklauskas et al. [29] for the detailed computational procedure. In this paper, a typical value of -200 $\mu\varepsilon$ was assumed and the calculated flexural cracking loads for VG1 and VG2 of S4, including the effect of concrete shrinkage, show better agreement with the experimental results as shown in **Fig. 9**.

Debernardi et al. [21] proposed an equation, which was a modified version of that provided by Model Code 1990 [30], for estimating the shear cracking load, V_{cr}:

$$V_{cr} = 0.15 \cdot \left(\frac{3 \cdot d}{M/V} \right)^{\frac{1}{3}} \cdot \left(1 + \sqrt{\frac{200}{d}} \right) \cdot \left(100 \cdot \rho_{st} \cdot f_{ck} \right)^{\frac{1}{3}} \cdot b_w \cdot d \tag{30}$$

where f_{ck} is in MPa. The predictions of V_{cr} with Eq. (30) are compared with the experimental results in **Fig. 10**. Eq. (30) indicates that the major parameters affecting the shear cracking loads include: (1) concrete compressive strength; (2) the web width; (3) the effective depth; (4) the moment-to-shear ratio; and (5) the tension reinforcement ratio. Therefore, the shear cracking loads of S1, S2 and S3 are illustrated in the same figure because they had the identical amounts of the aforementioned parameters. It can be found the expression proposed by Debernardi et al. [21] is capable of reproducing the experimental results.

4.3. Stirrup-yielding loads

The control of deflections at service load levels mainly involves the stage before the onset of stirrup-yielding. With regard to He Model as presented in Section 2.2, the stirrup-yielding load, V_y, is also needed for the estimation of the shear deformation. Consequently, it is necessary to determine V_y of the grids experimentally. In this section, the stirrup-yielding loads of the specimens will be estimated based on the experimental mean vertical strain.

The stress-strain curve of a bare steel re-bar is typically modelled as a elastic-perfectly plastic curve with a yield strain of $\varepsilon_{y,s}$ as shown in **Fig. 11**. However, in terms of the steel reinforcement surrounded by the concrete, the mean strain of the steel when the steel yields is different from $\varepsilon_{y,s}$ [31, 32]. **Fig. 11** illustrates a beam segment in the shear span with one stirrup at the onset of yielding. It could be found the strain varies along the stirrup, with higher levels at the cracks and lower levels between them. Once the strain of the stirrup at the cracks approaches $\varepsilon_{y,s}$, the mean strain of this stirrup (referred to as the apparent yield strain, $\varepsilon_{y,ap}$) is lower than $\varepsilon_{y,s}$. In this paper, the expression proposed by Belarbi and Hsu [32] was used to estimate the apparent yield strain of the steel surrounded by the concrete:

$$\begin{cases} f_{y,ap} = \left(0.93 - \dfrac{2}{\rho_s} \cdot \left(\dfrac{f_t}{f_y} \right)^{1.5} \right) \cdot f_y \\ \varepsilon_{y,ap} = \dfrac{f_{y,ap}}{E_s} \end{cases} \tag{31}$$

where $\varepsilon_{y,ap}$ and $f_{y,ap}$ are the apparent yield strain and the apparent yield stress of the steel surrounded by the concrete, respectively; f_y is the yield stress of the steel; E_s is the elastic modulus of the steel; and ρ_s is the steel reinforcement ratio.

The experimental stirrup-yielding loads of the grids of all specimens based on the concept of apparent yield strain and the measured mean vertical strain are listed in **Table 4**. The experimental results of the mean vertical strain along with the apparent stirrup-yielding strain could be found in Appendix A (see **Fig. A1** to **Fig. A4**) and **Fig. 25**. The minimum of V_y of all four grids represents the load level at the onset of the stirrup yielding in the shear span. It can be seen in **Table 4** that for specimen S4, no stirrup yielded during the loading procedure. The minimum stirrup-yielding loads of specimen S1, S3 and S5 were quite close to the peak load. In terms of S2 which had the lowest shear reinforcement ratio, the stirrups yielded first within VG2 and VG3 at the load level of 190 kN. **Table 4** also compares the values of V_y calculated using He Model with the experimental results. The calculated results constantly underestimate the actual stirrup-yielding loads.

4.4. Deflection results

The total deflection of the measuring zone in the shear span was determined by subtracting the vertical displacement of the target at the support from that at the bottom-right corner of the measuring zone (see **Fig. 3**). The shear-induced and flexure-induced deflection was determined by the methods presented in Section 3.3. The shear-induced deflection could also be obtained by subtracting the flexure-induced deflection from the total deflection. The experimental shear-induced deflections obtained by these two methods are compared in **Fig. 12**. Good agreement between the results from the two methods, which is contrary to that presented by Hansapinyo et al. [13] in which the traditional sensors were used, demonstrates the accuracy and superiority of the 3D-DIC technique in measuring the deformation of RC structures. The results of the virtual measuring grids in the two shear spans of specimen S1 and S3 were successfully recorded. The results of the shear-induced deflections in the two shear spans are compared in **Fig. 13** and acceptable repeatability of the test results could be seen. The presented results of specimen S1 and S3 hereafter in this paper are the averages of the two shear spans.

Fig. 14 illustrates the measured total deflections and those predicted using the expressions provided by ACI318-14 [2] (termed ACI Model) for which the shear deformation is ignored. It should be noted when calculating the deflection of S4 based on ACI Model, the concrete shrinkage of -200 $\mu\varepsilon$ was introduced by modifying the flexure cracking load. It indicates that ACI Model underestimates the deflections under service load which may bring un-conservative design. Underestimates of deflections with the ACI Model have also been shown by e.g. [33].

The experimental results of the flexure-induced deflections in the measuring zone are shown in **Fig. 15**. With identical cross sections and tension reinforcement, S1, S2, S3 and S5 had similar flexure-induced deflections (although S5 had larger web width, it made little difference in the flexural stiffness). The cracked flexure stiffness of S4 decreased faster than the other specimens due to its smaller amount of tension reinforcement. Discrepancy between the predictions with ACI Model and the measured results of the flexure-induced deflections could also be found in **Fig. 15**. This is attributed to the additional curvature induced by the shear force after shear cracking, which has been elaborated by Debernardi et al. [21], Hansapinyo et al. [13] and Ueda et al. [12]. JSCE Guidelines for Concrete 2007 [1] (termed JSCE Model) provided a model for predicting the flexure-induced deflection considering the additional curvature. The corresponding predictions are in good agreement with the experimental results as shown in **Fig. 15**.

The shear-induced deflections in the measuring zone of all specimens are presented in **Fig. 16**. By comparing the results of S1 and S2, the effect of stirrups on the shear deformation could be identified. S1 had a higher stirrup ratio than S2. The shear-induced deflection of S1 increased slower than that of S2 which is attributed to the restraints on the propagation of diagonal cracks imposed by the stirrups. The comparison between S1 and S3 indicates the stirrup spacing may have little influence on the shear deformation when the stirrup ratio keeps constant. It should be noted the stirrup spacing of S3 was 250 mm which conformed to the limitation of stirrup spacing specified by ACI318-14 [2] and Eurocode [5]. Whether the aforementioned conclusion holds true for the cases with larger amounts of the stirrup spacing which exceeds the codes provisions needs to be further investigated. S4 was reinforced by less tension reinforcement than S1 and had a larger shear-induced deflection than the reference beam. It implies the amount of tension reinforcement affects not only the flexure deformation but also the shear deformation. The reason might be that the tension reinforcement contributes to the restraint on the opening of shear cracks. The web width appears to be a critical factor influencing the shear deformation (comparing the results of S1 and S5). The larger web width brings the higher shear cracking loads. In addition, the slope of the shear force-shear deflection curve of S5 was steeper than that of S1, suggesting that the larger web width also contributes to the larger post-cracking tangent shear stiffness.

The shear-induced deflections of the specimens are given in comparison with the predictions with the available models presented in Section 2 (see **Fig. 17**). It should be noted that the experimental shear cracking loads were used when calculating the shear-induced deflections with the available models. Generally, all the predictions fail to match the experimental results. The use of Rahal Model overestimates the shear-induced deflections for all specimens while the predictions with other models are constantly smaller than the experimental results.

In **Fig. 17**, Eq. (13) proposed by He et al. [15] was used to predict the stirrup-yielding loads. As shown in **Table 4**, the experimental stirrup-yielding loads are smaller than the predictions with He Model. Consequently, the predicted shear-induced deflections with He Model are expected to be even smaller if the experimental results of V_y are used. However, as presented in He et al. [15], He Model was able to reproduce the shear deformation of several collected test beams. This conclusion should be treated with caution and the reasons are listed below:

(1) The effective shear depth of the beam, z, needed to be determined in He Model. As recommended by He et al. [15], its value was approximated by $0.9 \cdot d$ (d is the effective depth of the section). However, the corresponding values used for the specimens when verifying the model are questionable. For example, the beam specimens tested by Debernardi and Taliano [14] had a height of 600 mm and the effective depth was about 555 mm. Thus, the effective shear depth was

supposed to be around 500 mm while the selected value reported in [15] was only 350 mm. Additionally, the beam specimens tested by Cladera [34] had an effective depth of 353 mm and the corresponding effective shear depth should be 318 mm. By contrast, the value used by He et al. [15] was only 265 mm. The underestimates of the effective shear depth allow the predicted results of shear deformation to be irrationally larger.

(2) The selection of the elastic modulus of concrete is also questionable. For the beam specimens reported in Hansapinyo et al. [13], the elastic modulus was not directly tested. The cylinder concrete compressive strength was 33 MPa. He et al. [15] used 22 GPa instead as the elastic modulus of concrete, which was smaller than the estimations with the expressions proposed by the current codes, namely 31 GPa with Eurocode [5], 32 GPa with Model Code 2010 [4] and 27 GPa with ACI318-14 [2]. He et al. [15] did not make it clear why such a small amount of elastic modulus, which could irrationally increase the predicted shear-induced deflection, was selected.

(3) The calculation of shear deformation using He Model strongly depends on the choosing of the stirrup-yielding load, V_y. When verifying the model, the values of V_y were reported to be based on the experimental results [15]. For the beams tested by Debernardi and Taliano [14], the "experimental" results of V_y were taken as 200 kN and 240 kN for TR2 and TR6 in He et al. [15], respectively. However, Debernardi and Taliano [14] did not report the experimental V_y. 200 kN and 240 kN were just the peak loads given in the shear force - shear strain curves of these two beams.

(4) He et al. [15] predicted the shear strain of two grids of two restrained beams tested by themselves. The experimentally observed shear cracking loads were

reported to be 80 kN and used to verify He Model. However, another paper [16], which also presented the experimental results of the identical experimental program, reported 150 kN for the shear cracking loads. The contradiction between these two reported test results implies the validity of He Model is still inconclusive.

In order to examine the reason why the other models (i.e. JSCE Model, Ueda Model, Deb Model, Han Model, Rahal Model) are unable to produce satisfactory predictions of the shear-induced deflections, it is helpful to further examine the deformation results of the grids, i.e. the mean shear strain, the principal compressive strain angle, the principal compressive strain, the mid-depth longitudinal strain and the mean vertical strain. Also, the collected experimental results from the literature may also be beneficial to the assessment of the prediction models. The discussion will be presented in the subsequent sections.

5. Assessing the available models based on the experimental results in this paper

Before the assessment, it may be helpful to identify the region (i.e. B-region or D-region) to which each measuring grid belongs. As shown in **Fig. 4**, the amounts of the vertical strain in the vicinity of either the loading point or the support were significantly smaller than those in the middle third of the shear span. It is attributed to the vertical stress induced by the concentrated loads which disturb the stress and strain distribution. This region is termed the D-region where D stands for disturbance while the B-region (B stands for Bernoulli) refers to the area which is not influenced by the concentrated loads [27]. Regarding the beam specimens studied in this paper, the length of the D-regions was taken as the height of the cross section and the extent of the B-region and D-region in the shear span is illustrated in **Fig. 3**(a). VG1 and VG4 were considered to be within the D-region while VG2 and VG3 within the B-region.

5.1. Mean shear strain of the grids

Fig. 18 shows the experimental mean shear strain of the grids with varied moment-to-shear ratios of specimen S3. The dash lines represent the levels of the shear cracking loads. It was evident that the increase of the shear strain with the rise of the load level became faster after shear cracks formed. By comparing the mean shear strain of VG2 and VG3 illustrated in **Fig. 18**, it could be found that at the same shear level, the mean shear strain was larger when the moment was larger. Similar results could be observed when it comes to the other specimens (see **Fig. A5** in Appendix A for details). Debernardi and Taliano [14] also discovered the effect of the moment on the shear deformation. It is also of interest to note that this conclusion is not applicable when comparing the shear strain of VG1 in the D-region and VG2 in the B-region. Although VG1 had a higher moment-to-shear ratio, its shear strain was not noticeably larger than that of VG2. Opposite phenomenon could even be observed regarding specimen S1 and S5 (see **Fig. A5** in Appendix A). Further investigation is needed to gain insight into the variation of the mean shear strain with the moment-to-shear ratio in the D-region.

It can be assumed that the tangent shear stiffness, K_t, remains constant after shear cracking based on the observation of the experimental results of the shear force – mean shear strain (V-γ) curves. After the stirrups yield, the shear stiffness is believed to degrade further owing to the stiffness degradation of the stirrups after yielding. As this paper deals with the serviceability limit sates (namely, the shear force level lower than V_y), the experimental tangent shear stiffness after shear cracking was then obtained by performing linear regression of the V-γ curve between the shear cracking load (V_{cr}) and the stirrup-yielding load (V_y) in which V_{cr} and V_y were quantified based on the experimental results (see **Table 3** and **Table 4** for the values). Similarly, the predicted tangent shear stiffness after shear cracking with the available models was obtained.

Table 5 gives the experimental and calculated K_t of the grids located in the B-region of the beams in this paper. It can be seen that the tangent shear stiffness decreased as the value of M/Vh increased, i.e. the effect of moment on the amount of K_t. However, as shown in **Table 5**, JSCE Model, Ueda Model and Rahal Model do not take such effect into account. The predictions with JSCE Model, Ueda Model and Han Model are significantly larger than the experimental results. The calculated values of the tangent shear stiffness after shear cracking with Deb Model were constantly larger than the experimental results. The corresponding average of the calculated value-to-experimental value ratios was 1.31. With regard to Rahal Model, the predictions were constantly smaller. The average of the ratios of the calculated values to the experimental values was 0.71.

5.2. Principal compressive strain angles of the grids

In terms of the available models based on either the truss analogy or the MCFT (i.e. JSCE Model, Ueda Model and Deb Model), the inclination of the diagonal concrete struts is a critical parameter for estimating the mean shear strain as well as the mean vertical strain, the mid-depth longitudinal strain and the principal compressive strain. Although several expressions have been developed to estimate the angle as presented in Section 2, related experimental results were limited so that the validity of these expressions remained unknown. Generally, the assumption that the inclination of the diagonal concrete struts equals the principal compressive strain angle is accepted when dealing with the cracked concrete [14, 15, 35, 36]. In this section, the experimental principal compressive strain angles of the grids will be presented and compared with the predictions with several available models.

Fig. 19 illustrates the principal compressive strain angles of the grids with different moment-to-shear ratios in specimen S1. Only the results after shear cracking are illustrated in this figure. It could be found that the angle kept decreasing after the formation of shear cracks. The variation of the angle with the moment-to-shear ratio is also evident. Comparing the results of VG2 and VG3 in the B-region, it can be seen that a larger moment-to-shear ratio caused a larger amount of the principal compressive strain angle at the same shear force.

The influence of the stirrup ratio and the tension reinforcement ratio on the principal compressive strain angle is illustrated in **Fig. 20**. Placing smaller amounts of stirrups caused the decline in the value of principal compressive strain angle which could be identified by the comparison between S1 and S2. By comparing the results of S1 and S4, the influence of tension reinforcement could be identified. Less tension reinforcement caused the growth in the value of the angle at relative high levels of the shear forces.

Fig. 21 shows the predictions of the angles of the grids in specimen S1 using the following models: JSCE Model, Ueda Model and Deb Model. It could be concluded that none of these three models is able to reproduce the variation of the angles with the shear force levels for the grids in the D-region. This conclusion holds true for all the other specimens tested in this paper (see **Fig. A6** to **Fig. A9** in Appendix A). As illustrated in **Fig. 21** and **Fig. A6** to **Fig. A9** in Appendix A, although certain models are capable of reproducing the angles of certain grids in the B-region (e.g. the predictions with JSCE Model agree well with the experimental results of VG2 in S1, VG2 in S3 and VG3 in S4 while those with Ueda Model agree well with the experimental results of VG2 in S2, VG3 in S3 and VG3 in S5), none of them could produce satisfactory predictions for all the specimens with varied design parameters.

5.3. Principal compressive strain of the grids

In terms of JSCE Model, Ueda Model and Deb Model, the strain of the diagonal concrete strut, i.e. principal compressive strain, ε_2, is required. For JSCE Model and Ueda Model, the expressions of ε_2 are the same (see Eq. (10)). The expression provided by Deb Model is similar to that of JSCE Model and Ueda Model but with a minor difference (see Eq. (17)). As mentioned in Section 5.2, the available models are not able to predict the experimental principal compressive strain angles accurately. In order to check the expressions for estimating ε_2 without introducing the effect from the deviation of the calculated angles, the experimental θ was used to calculate the values of ε_2. The experimental results of θ will also be used when checking the expressions for the mid-depth longitudinal strain and the mean vertical strain presented in Section 5.4 and 5.5, respectively. Additionally, when the shear force level was below the shear cracking load, the response was assumed to be elastic.

Fig. 22 shows the experimental and calculated principal compressive strain of the grids in specimen S3. It could be found that after shear cracking, the principal compressive strain increased faster than the elastic response. Both Eq. (10) and Eq. (17) produce acceptable results of the trends in the development of the principal compressive strain of the grids. The expression provided by Deb Model (i.e. Eq. (17)) appears to predict ε_2 more accurately.

5.4. Mid-depth longitudinal strain of the grids

The mid-depth longitudinal strain, ε_x, is required when using Deb Model to estimate the mean shear strain as presented in Section 2.3. The expressions for estimating ε_x (i.e. Eq. (15) and Eq. (16)) are applicable only to the grids in the B-region as they are derived based on the plane-section assumption. The experimental and calculated ε_x of VG3s in S1 are presented in **Fig. 23**. The predictions termed Pure Bend in **Fig. 23** refer to the results estimated based on the pure bending theory in which the influence of shear is ignored. As shown in **Fig. 23**, the predictions based on the pure bending theory deviate significantly from the experimental results after shear cracking. Although the influence of shear on the longitudinal strain has been taken into account in Deb Model, the estimates of ε_x remain lower than the experimental results after shear cracking. Similar results could be found with respect to the mid-depth longitudinal strain of VG3s in the other specimens (see **Fig. A10** in Appendix A)

Through the observation of experimental results, the expression of ε_x provided by Deb Model was modified accordingly as presented below:

$$\begin{cases} \varepsilon_x = \dfrac{\varepsilon_{top} + \varepsilon_{bot}}{2} \\ \varepsilon_{top} = \left[M + \dfrac{V}{2} \cdot 0.9 \cdot d \cdot \cot\theta \right] \cdot \dfrac{d - x_c}{E_c \cdot I_e} \\ \varepsilon_{bot} = \left[-M + \dfrac{V}{2} \cdot 0.9 \cdot d \cdot \cot\theta \right] \cdot \dfrac{x_c - 0.1 \cdot d}{E_c \cdot I_e} \end{cases} \tag{32}$$

The predictions with Eq. (32) are closer to the experimental results as shown in **Fig. 23** and **Fig. A10** in Appendix A. In this section, a preliminary "Modified" Deb Model was developed in which θ was determined based on the experimental results, ε_x determined with Eq. (32) and ε_2 determined with Eq. (17). The mean shear strain was then estimated with Eq. (14). The calculated results with the "Modified" Deb Model are presented in **Fig. 24**. Good agreement between the experimental and calculated results is observed. However, it should be noted that this model is just a preliminary model in which the critical parameter, θ, must be obtained from the experiments. It seems not possible to derive a reliable model for θ based on the limited experimental results presented in this paper. Further research is needed.

5.5. *Mean vertical strain of the grids*

The mean vertical strain, ε_y, is also a key parameter when estimating the shear deformation with either JSCE Model or Ueda Model based on the truss analogy. In these two models, the expressions for estimating ε_y are the same (see Eq. (7), Eq. (8) and Eq. (9)) and the effect of the concrete surrounding the stirrup is taken into consideration by the term $E_c \cdot A_{ce}$ where A_{ce} is the effective area of the concrete around the stirrups. The predicted results of the grids in specimen S1 based on the JSCE Model and the Ueda Model are compared with the measured results in **Fig. 25**. In addition, the predictions with a similar expression based on the truss analogy but omitting the effect of the concrete (i.e. removing the term $E_c \cdot A_{ce}$ in Eq. (7)) are illustrated in **Fig. 25** as well, which is termed Pure Truss Model. The expression is given:

$$\varepsilon_y = \frac{(V - V_{cr}) \cdot s_w}{E_{sw} \cdot A_{sw} \cdot 0.9 \cdot d \cdot \cot\theta} \tag{33}$$

As shown in **Fig. 25**, the mean vertical strain was negligible before shear cracking and then kept growing as the shear force increased. For the grids in the B-region, i.e. VG2 and VG3, the expressions provided by JSCE Model and Ueda Model underestimate the mean vertical strain. The Pure Truss Model, which excludes the effect of the concrete, produces larger vertical strain than the experimental results of VG2. However, with respect to VG3, the predictions with Pure Truss Model are consistent with the measured mean vertical strain. Similar results could also be discovered for all the other specimens (see **Fig. A1** to **Fig. A4** in Appendix A). It seems that for the grids in the B-region with lower moment-to-shear ratios, i.e. VG3s, the effect of the concrete surrounding the stirrups is negligible while for those with higher moment-to-shear ratios, i.e. VG2s, this effect could not be neglected. In other words, the moment-to-shear ratios might affect the tension stiffening effect of the concrete around the stirrups. For the grids in the D-region, i.e. VG1 and VG4, Pure Truss Model overestimates the mean vertical strain. Despite accounting for the tension stiffening effect, JSCE Model and Ueda Model still provide larger mean vertical strain of VG1 than the experimental results. With respect to the D-region in RC beams, not only the truss mechanism but also the arch mechanism [37] is known to play a role in the shear resistance. Therefore, part of the external shear force causes the increase of the mean vertical strain through the truss mechanism while the remaining reduces the vertical deformation through the arch mechanism. The results of the other specimens are similar as illustrated in **Fig. A1** to **Fig. A4** in Appendix A. In general, the available models are not capable of predicting the development of the mean vertical strain at different sections in the shear span of RC beams.

6. Assessing the available models based on the collected experimental results

The experimental mean shear strain of 18 more grids of RC beams were collected from the literature [14, 15, 17] aimed at assessing the available models in terms of predicting the shear deformation of the grids in the B-region. The material and section properties of the collected specimens are summarized in **Table 5**.

The beam specimens reported by Vecchio and Collins [17] and He et al. [15] were restrained beams for which the mean shear strain near the contraflexure point were directly measured. The values of M/Vh for these grids were all below 1 (see **Table 5**). Debernardi and Taliano [14] measured the mean shear strain of the grids with various M/Vh from 1.7 up to 4.8. The values of the experimental tangent shear stiffness after shear cracking, K_t, for the collected data were estimated in the same way as presented in Section 5.1. The shear cracking load, V_{cr}, was determined with the expression proposed by Debernardi et al. [21] (see Eq. (30)). As the stirrup-yielding loads, V_y, of the collected beams were not reported, the values of V_y were estimated as $0.7 \cdot V_{peak}$ where V_{peak} represents the peak shear force. $0.7 \cdot V_{peak}$ is commonly assumed to be the service load level at which the stirrups are thus considered to be elastic.

The values of the experimental K_t of the collected RC beams are compared with the calculated values with the available models in **Table 5**. It can be seen that JSCE Model, Ueda Model and Han Model significantly overestimate not only the shear stiffness of the beams tested in this paper, but also of the beams collected from the literature. On average, the predictions of K_t with Deb Model are 24 percent larger than the experimental results while Rahal Model underestimates the experimental K_t by 24 percent. However, regarding the mean shear strain near the point of contraflexure (i.e. the experimental results reported by Vecchio and Collins [17] and He et al. [15]), the predictions with Deb Model deviate considerably from the experimental results. The average of the calculated value-to-experimental value ratios (abbr. CV/EV) is 1.94. It appears that Deb Model produces poorer predictions of the shear deformation near the point of contraflexure than elsewhere. On the contrary, Rahal Model is able to produce acceptable predictions of the mean shear strain near the contraflexure point (average CV/EV = 0.87) despite the fact that it underestimates the shear deformation elsewhere (average CV/EV = 0.73).

7. Conclusion

An experimental program concerning the shear deformation of five RC beams with thin webs using the Digital Image Correlation (DIC) technique is presented in this paper. The experimental results presented in this study, as well as others collected from the literature were used to assess the available models for predicting the shear deformation after shear cracking. The following conclusions can be drawn from the above analysis and discussion:

- The 3D-DIC technique accompanied by the water-transfer-printing random speckles could be a reliable non-contact measuring approach for monitoring the full-field displacement and strain in the large-scale regions of concrete structures. Compared with traditional sensors, the measured shear deformation with 3D-DIC technique and virtual measuring grids were more accurate and reliable. The experimental shear-induced deflections in the two identical shear spans indicated acceptable repeatability of the measured data.
- The use of the expressions proposed by ACI318-14 [2] significantly underestimated the total deflection of the specimens tested in this paper. The flexure-induced deflection of these specimens were well predicted by the expressions proposed by JSCE [1] in which the influence of shear on the flexure deformation is considered.
- The following parameters may influence the shear deformation of RC beams after shear cracking: (1) the stirrup ratio; (2) the tension reinforcement ratio; and (3) the web width. It appears the stirrup spacing have little influence on the shear-induced deflections.
- The moment-to-shear ratio, the tension reinforcement ratio, the stirrup ratio and the shear force level had influence on the inclination of the diagonal concrete struts. None of the current models was capable of reproducing the inclination of the struts of the test beams in this paper.
- An expression based on the model developed by Debernardi et al. [21] with a minor modification was developed to better estimate the mid-depth longitudinal strain of the grids of the test beams after shear cracking.
- It appears that the moment-to-shear ratio influences on the tension stiffening effect of concrete around the stirrups in the B-region after shear cracking. For

the grids in the D-region, part of the external shear force seems to be balanced by the arch mechanism so that the vertical strain induced by the truss mechanism is reduced. None of the available models based on the truss analogy could provide accurate predictions of the mean vertical of the test beams in this paper.

- The experimental results in this study and those collected from the literature indicated the tangent shear stiffness of the grids in the B-region after shear cracking was lower when the moment-to-shear ratio was larger. The available prediction models were not able to predict the post-shear cracking shear deformation of the RC beams presented in this study and collected from the literature.

8. Acknowledgements

The authors gratefully acknowledge financial support from National Natural Science Foundation of China (No. 51378104) and A Project Funded by the Priority Academic Program Development of Jiangsu Higher Education Institutions. The first author's stay in Sweden was partly facilitated by the Development Fund of the Swedish Construction Industry (SBUF), the Swedish Research Council Formas and Elsa and Sven Thysell Foundation. The authors would also like to thank others who provided help during the research program, including Dr. Shoutan Song, Ph.D. students Shuai Dong, Shanshan Yu and Xiangyang Xu (all from SEU) for helping with the DIC measurements.

9. Appendix A

The experimental and calculated mean vertical strain of the grids of specimen S2 to S5 are illustrated in **Fig. A1** to **Fig. A4**.

The experimental mean shear strain of the grids of all specimens are illustrated in **Fig. A5**.

The experimental and calculated principal compressive strain angles of the grids of specimen S2 to S5 are illustrated in **Fig. A6** to **Fig. A9**.

The experimental and calculated mid-depth longitudinal strain of VG3 in specimen S2 to S5 are illustrated in **Fig. A10**.

10. References

[1] JSCE. Standard Specifications for Concrete Structures - 2007 - Design. Tokyo, Japan: JSCE (Japan Society of Civil Engineers); 2007.

[2] ACI. Building Code Requirements for Structural Concrete (ACI318M-14) and Commentary. Farmington Hill, MI: ACI (American Concrete Institute); 2014.

[3] AASHTO. AASHTO LRFD Bridge Design Specifications, 4th ed. Washington, DC: AASHTO (American Association of State Highway and Transportation Officials); 2007.

[4] fib. fib Model Code for Concrete Structures 2010. Switzerland: fib (International Federation for Structural Concrete); 2010.

[5] CEN. Eurocode 2: Design of Concrete Structures-Part 1-1: General Rules and Rules for Buildings. Brussels: CEN (European Committee for Standardization); 2004.

[6] Kamaitis Z, Kamaitis Z. THE CAUSES OF SHEAR CRACKING IN PRESTRESSED CONCRETE BOX-GIRDER BRIDGES. Statyba. 1996;2:26-34.

[7] Ma J. Strengthening of San-Meng-Xia-Yellow-River highway bridge (in Chinese). Highway. 2004;1:62-4.

[8] Malm R. Shear cracks in concrete structures subjected to in-plane stresses. Stockholm: Royal Institute of Technology (KTH); 2006.

[9] Feng RS. Study on the Factors and Control Strategy on the Deflection of PC Rigid-Frame Bridges (in Chinese). Chongqing: Chongqing Jiaotong University; 2010.

[10] ACI. Control of Deflection in Concrete Structures. American Concrete Institute; 2003.

[11] Huang Z, Lü Z, Song S, Tu Y, Blanksvärd T, Sas G et al. Finite element analysis of shear deformation in reinforced concrete shear-critical beams. Structure and Infrastructure Engineering. 2018;14:791-806.

[12] Ueda T, Sato Y, Ito T, Nishizone K. Shear Deformation of Reinforced Concrete Beam. Journal of Materials Concrete Structure Pavements, JSCE. 2002;56:9-23.

[13] Hansapinyo C, Pimanmas A, Maekawa K, Chaisomphob T. Proposed Model of Shear Deformation of Reinforced Concrete Beam after Diagonal Cracking. Journal of Materials Concrete Structure Pavements, JSCE. 2003;58:305-19.

[14] Debernardi PG, Taliano M. Shear Deformation in Reinforced Concrete Beams with Thin Web. Magazine of Concrete Research. 2006;58:157-71.

[15] He Z-Q, Liu Z, Ma ZJ. Shear Deformations of RC Beams under Service Loads. Journal of Structural Engineering. 2017;143:04016153.

[16] Zheng K, Liu Z, Qin S, Zhou M. Analytical Model for Shear Stiffness of Reinforced Concrete Beam with Stirrups (in Chinese). Chinese Journal of Theoretical and Applied Mechanics. 2016;48:1136-44.

[17] Vecchio FJ, Collins MP. Predicting the Response of Reinforced-Concrete Beams Subjected to Shear Using Modified Compression Field-Theory. Aci Struct J. 1988;85:258-68.

[18] Jin Ff. Time-Dependent Behaviour of RC Beams Strengthened with Pre-stressed CFRP Straps. Cambridge, UK: Cambridge University; 2016.

[19] Pan ZF, Li B, Lu ZT. Effective shear stiffness of diagonally cracked reinforced concrete beams. Eng Struct. 2014;59:95-103.

[20] Wang T, Dai JG, Zheng JJ. Multi-Angle Truss Model for Predicting the Shear Deformation of RC Beams with Low Span-Effective Depth Ratios. Eng Struct. 2015;91:85-95.

[21] Debernardi PG, Guiglia M, Taliano M. Shear Strain in B-Regions of Beams in Service. Eng Struct. 2011;33:368-79.

[22] Rahal KN. Post-cracking shear modulus of reinforced concrete membrane elements. Eng Struct. 2010;32:218-25.

[23] Sas G, Blanksvard T, Enochsson O, Taljsten B, Elfgren L. Photographic Strain Monitoring During Full-Scale Failure Testing of Ornskoldsvik Bridge. Structural Health Monitoring. 2012;11:489-98.

[24] Mahal M, Blanksvärd T, Täljsten B, Sas G. Using digital image correlation to evaluate fatigue behavior of strengthened reinforced concrete beams. Eng Struct. 2015;105:277-88.

[25] Popescu C, Sas G, Sabau C, Blanksvärd T. Effect of Cut-Out Openings on the Axial Strength of Concrete Walls. Journal of Structural Engineering. 2016;142:04016100.

[26] Sabau C, Gonzalez-Libreros JH, Sneed LH, Sas G, Pellegrino C, Täljsten B. Use of image correlation system to study the bond behavior of FRCM-concrete joints. Materials and Structures. 2017;50:172.

[27] Schlaich J, Schafer K, Jennewein M. Toward a Consistent Design of Structural Concrete. J Prestr Concrete I. 1987;32:74-150.

[28] Zhenning C, Chenggen Q, Feipeng Z, Xiaoyuan H. A method to transfer speckle patterns for digital image correlation. Measurement Science and Technology. 2015;26:095201.

[29] Kaklauskas G, Gribniak V, Bacinskas D, Vainiunas P. Shrinkage influence on tension stiffening in concrete members. Eng Struct. 2009;31:1305-12.

[30] CEB-FIP. CEB-FIP Model Code 1990. Lausanne, Switzerland: CEB-FIP (Comite Euro-International du Beton); 1993.

[31] Maekawa K, Pimanmas A, Okamura H. Nonlinear Mechanics of Reinforced Concrete. London: Spon Press; 2003.

[32] Belarbi A, Hsu TTC. Constitutive Laws of Concrete in Tension and Reinforcing Bars Stiffened by Concrete. Aci Struct J. 1994;91:465-74.

[33] Scordelis AC, Elfgren LG, Larsen PK. Time-Dependent Behavior of Concrete Box Girder Bridges. ACI Journal Proceedings. 1979;76:159-78.

[34] Cladera A. Shear Design of Reinforced High-Strength Concrete Beams. Barcelona: University of the Balearic Islands; 2003.

[35] Vecchio FJ, Collins MP. The Modified Compression-Field Theory for Reinforced-Concrete Elements Subjected to Shear. ACI Journal. 1986;83:219-31.

[36] Pang XB, Hsu TTC. Behavior of Reinforced Concrete Membrane Elements in Shear. Aci Struct J. 1995;92:665-79.

[37] Qi JN, Wang JQ, John Z, Tong T. Shear Behavior of Externally Prestressed Concrete Beams with Draped Tendons. Aci Struct J. 2016;113:677-88.

Table 1 Details of the specimens in the experimental program

Beam	Span (mm)	Shear span (mm)	Height (mm)	Web width (mm)	Tension steel[a]	Top steel	Stirrup[b]	Test variable
S1	5000	2250	600	100	8D20 (4.53%)	3D20	D8@150 (0.67%)	Reference beam
S2	5000	2250	600	100	8D20 (4.53%)	3D20	D6@150 (0.38%)	Stirrup ratio
S3	5000	2250	600	100	8D20 (4.53%)	3D20	D10@250 (0.63%)	Stirrup spacing
S4	5000	2250	600	100	5D20 (2.83%)	3D20	D8@150 (0.67%)	Tension steel ratio
S5	5000	2250	600	150	8D20 (3.02%)	3D20	D8@150 (0.45%)	Web width

[a]The percentages in the brackets represent the tension reinforcement ratio

[b]The percentages in the brackets represent the stirrup ratio

Table 2 Mechanical properties of the steel reinforcement.

Reinforcement	Diameter (mm)	Area (mm^2)	Yield stress (MPa)	Tensile stress	Modulus of elasticity (GPa)
D6	6	28.3	431	558	201 GPa
D8	8	50.3	450	572	205 GPa
D10	10	78.5	446	549	199 GPa
D20	20	314.2	440	560	200 GPa

Table 3 Cracking loads of all virtual measuring grids of the beam specimens

Beam	VG1		VG2		VG3		VG4	
	FCL[a]	SCL[b]	FCL[a]	SCL[b]	FCL[a]	SCL[b]	FCL[a]	SCL[b]
S1	50 kN	70 kN	65 kN	80 kN	--[c]	90 kN	--[c]	140 kN
S2	60 kN	70 kN	70 kN	90 kN	--[c]	100 kN	--[c]	140 kN
S3	50 kN	65 kN	70 kN	75 kN	--[c]	105 kN (120 kN)[d]	--[c]	140 kN (160 kN)[d]
S4	35 kN	55 kN	45 kN	65 kN	--[c]	80 kN	--[c]	100 kN
S5	50 kN	90 kN	75 kN	105 kN	--[c]	115 kN	--[c]	180 kN

[a]FCL represents flexural cracking load.
[b]SCL represents shear cracking load.
[c]"--" means no flexural cracking was observed in the test.
[d]The values in the brackets are the shear cracking loads of the grids in the left shear span.

Table 4 Stirrup-yielding loads of the grids of the beam specimens

Beam	V_{peak} (kN)[a]	$V_{y,cal}$ (kN)[b]	$\varepsilon_{y,ap}$ of stirrups	Grid	$V_{y,exp}$ (kN)	Min. $V_{y,exp}$ (kN)[c]	$V_{y,cal}$/min. $V_{y,exp}$
S1	260	207	0.00156	VG1	--[d]	245	0.83
				VG2	245		
				VG3	250		
				VG4	--[d]		
S2	260	143	0.00119	VG1	210	190	0.75
				VG2	190		
				VG3	190		
				VG4	255		
S3	265	198	0.00153	VG1	265	235	0.84
				VG2	235		
				VG3	235		
				VG4	--[d]		
S4	157.5	207	0.00156	VG1	--[d]	--[d]	--[d]
				VG2	--[d]		
				VG3	--[d]		
				VG4	--[d]		
S5	255	238	0.00132	VG1	--[d]	250	0.95
				VG2	250		
				VG3	--[d]		
				VG4	--[d]		

[a] V_{peak} is the peak load of the beam specimen.
[b] $V_{y,cal}$ is the calculated stirrup-yielding load with He Model as presented in Section 2.2.
[c] Min. $V_{y,exp}$ is the minimum of the experimental stirrup-yielding loads of all four grids. It represents the load level at which the first stirrup in the shear span starts yielding.
[d] "--" means no stirrup-yielding was observed in the test.

Table 5 Tangent shear stiffness after shear cracking of the grids in the B-region

Literature	Beam	f_c (MPa)	b_w (mm)	h (mm)	ρ_{st}	ρ_{sw}	M/Vh	Experimental K_t (kN)	Calculated K_t (kN)					Calculated value/Experimental value				
									JSCE Model	Ueda Model	Deb Model	Han Model	Rahal Model	JSCE Model	Ueda Model	Deb Model	Han Model	Rahal Model
This paper	S1	40.0	100	600	4.53%	0.67%	1.3	68100	141000	166000	91900	156000	47400	2.07	2.44	1.35	2.29	0.70
							2.2	62300	141000	166000	87500	132000	47400	2.26	2.66	1.40	2.12	0.76
	S2	40.0	100	600	4.53%	0.38%	1.3	59100	137000	145000	79000	137000	35600	2.32	2.45	1.34	2.32	0.60
							2.2	52000	137000	145000	75500	115000	35600	2.63	2.79	1.45	2.21	0.68
	S3	40.0	100	600	4.53%	0.63%	1.3	74600	136000	158000	90500	153000	45800	1.82	2.12	1.21	2.05	0.61
							2.2	71400	136000	158000	86700	129000	45800	1.90	2.21	1.21	1.81	0.64
	S4	40.0	100	600	2.83%	0.67%	1.3	58600	197000	190000	78300	159000	47400	3.36	3.24	1.34	2.71	0.81
							2.2	52300	197000	190000	67000	131000	47400	3.77	3.63	1.28	2.50	0.91
	S5	40.0	150	600	3.02%	0.45%	1.3	84000	260000	255000	108000	221000	58000	3.10	3.04	1.29	2.63	0.69
							2.2	83100	260000	255000	102000	176000	58000	3.13	3.07	1.23	2.12	0.70
Vecchio and Collins [17]	SK3	28.7	305	610	2.45%	0.47%	0.0	102000	269000	401000	211000	423000	100000	2.64	3.93	2.07	4.15	0.98
	SK4	28.7	184	610	4.07%	0.77%	0.0	102000	164000	256000	154000	283000	77700	1.61	2.51	1.51	2.77	0.76
	SM1	29.0	153	610	2.73%	0.53%	0.0	51900	121000	187000	117000	220000	55800	2.33	3.60	2.25	4.24	1.08
	SP0	25.0	153	610	2.73%	0.62%	0.0	74100	114000	173000	112000	217000	52900	1.54	2.33	1.51	2.93	0.71
He et al. [15]	S0.4	38.4	100	800	4.79%	0.40%	0.4	52100	172000	247000	113000	199000	42600	3.30	4.74	2.17	3.82	0.82
	S0.5	38.4	100	800	4.79%	0.50%	0.4	53400	210000	282000	122000	209000	47600	3.93	5.28	2.28	3.91	0.89
Debernardi et al. [14]	TR1	22.0	100	600	1.81%	0.51%	1.7	47900	158000	168000	36300	106000	35800	3.30	3.51	0.76	2.21	0.75
							2.5	38700	158000	168000	32800	85900	35800	4.08	4.34	0.85	2.22	0.93
	TR2	22.0	100	600	3.24%	0.51%	1.7	52900	126000	114000	52400	103000	35800	2.38	2.16	0.99	1.95	0.68
							2.5	46300	126000	114000	48700	88800	35800	2.72	2.46	1.05	1.92	0.77
	TR3	20.0	100	600	1.81%	0.51%	2.1	46700	162000	161000	33400	97600	34300	3.47	3.45	0.72	2.09	0.73
							2.9	40300	162000	161000	29800	82300	34300	4.02	4.00	0.74	2.04	0.85
	TR5	31.0	100	600	1.81%	0.51%	2.0	64600	161000	162000	41600	104000	41800	2.49	2.51	0.64	1.61	0.65
							4.0	55800	161000	162000	35700	89900	41800	2.89	2.90	0.64	1.61	0.75
							4.8	55800	161000	162000	35200	82600	41800	2.89	2.90	0.63	1.48	0.75
	TR6	35.6	100	600	3.24%	0.51%	2.0	70700	141000	136000	64700	110000	44400	1.99	1.92	0.92	1.56	0.63
							4.0	60600	141000	136000	56900	99300	44400	2.33	2.24	0.94	1.64	0.73
							4.8	56800	141000	136000	57800	93100	44400	2.48	2.39	1.02	1.64	0.78
Average														2.74	3.03	1.24	2.38	0.76
Standard deviation														0.72	0.85	0.48	0.79	0.11

Note: f_c is the cylinder compressive strength of concrete; b_w is the web width; h is the beam height; ρ_{st} is the tension reinforcement ratio; ρ_{sw} is the stirrup ratio; M/Vh is the moment-to-shear ratio over the beam height; and K_t is the tangent shear stiffness after shear cracking.

Fig. 1 Details of the beam specimens

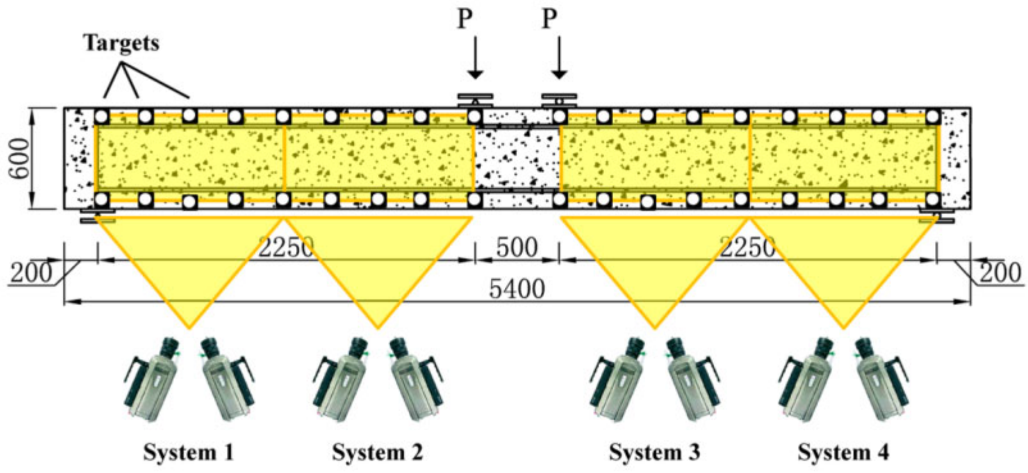

(a) Elevation of specimens

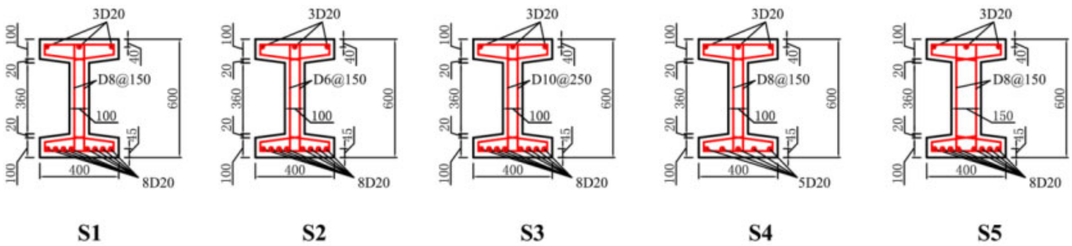

(b) Cross sections of specimens

Fig. 2 General view of the test setup and the instrumentation

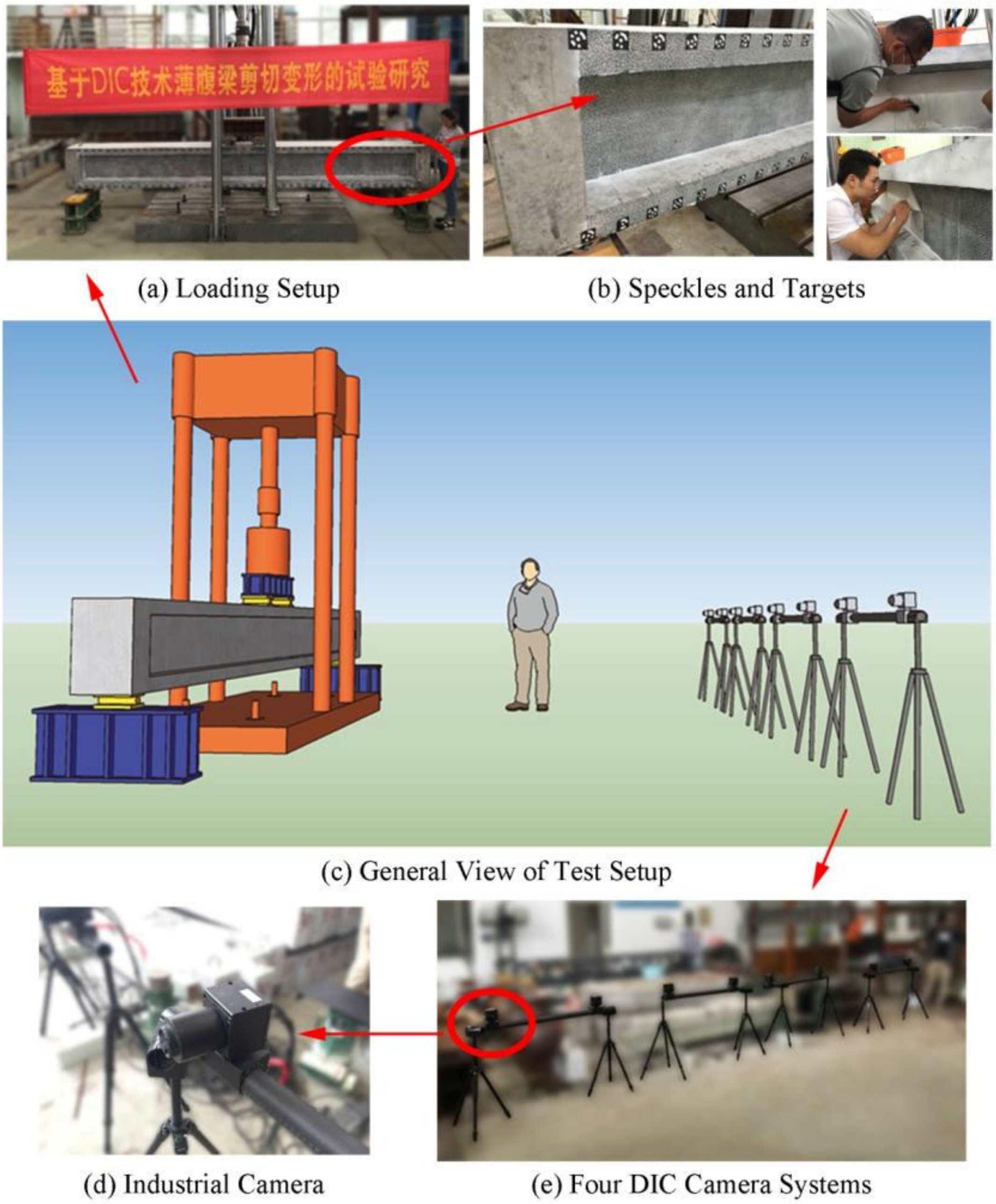

Fig. 3 Schematic diagram of the virtual measuring grids

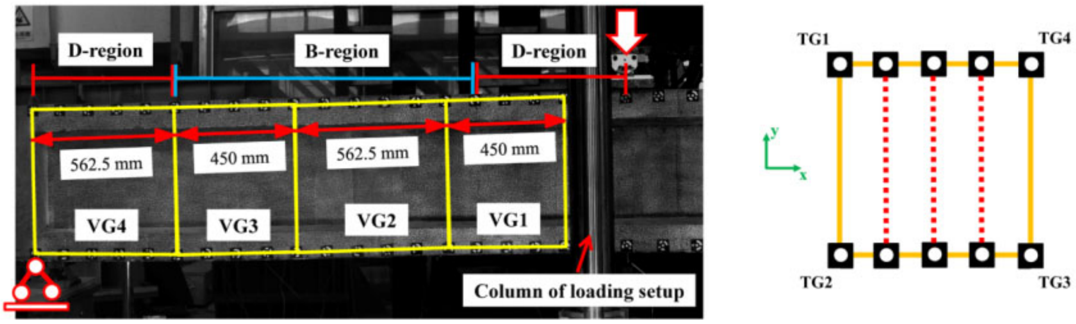

(a) Arrangement of virtual measuring grids (b) Virtual measuring grid

Fig. 4 Vertical strain distribution in the right shear span of S1 at the shear force level of 150 kN

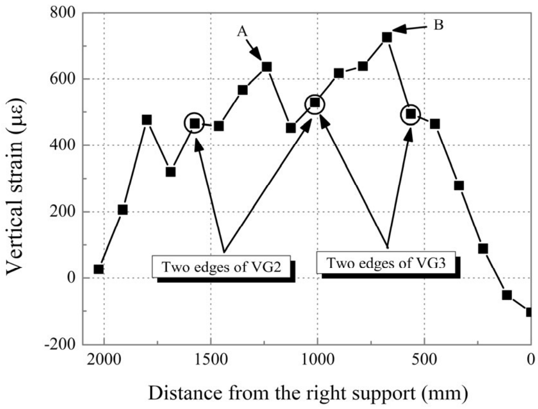

Fig. 5 Crack pattern in the right shear span of S1 at the shear force level of 150 kN

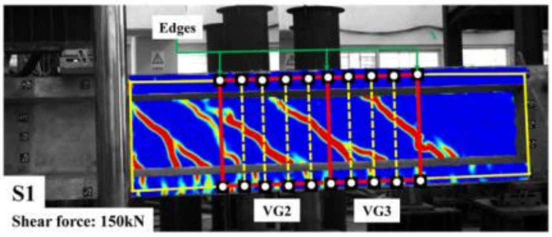

Fig. 6 Typical failure mode of the beam specimens

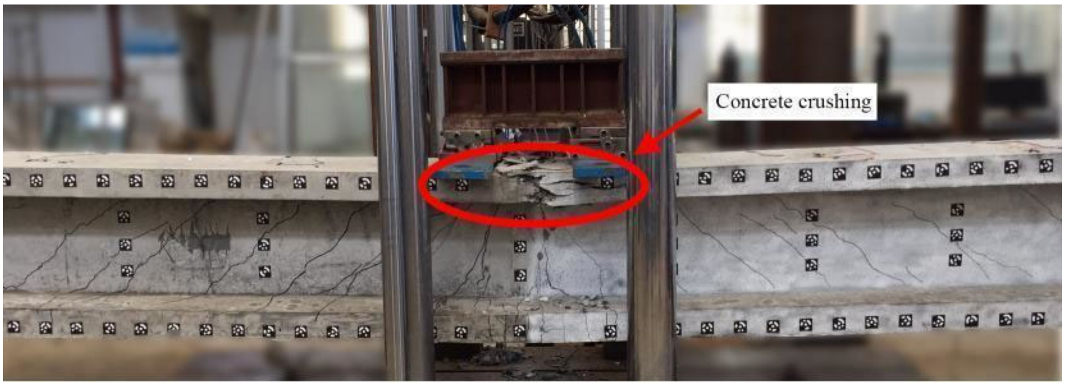

Fig. 7 Crack pattern of S4 at the peak load

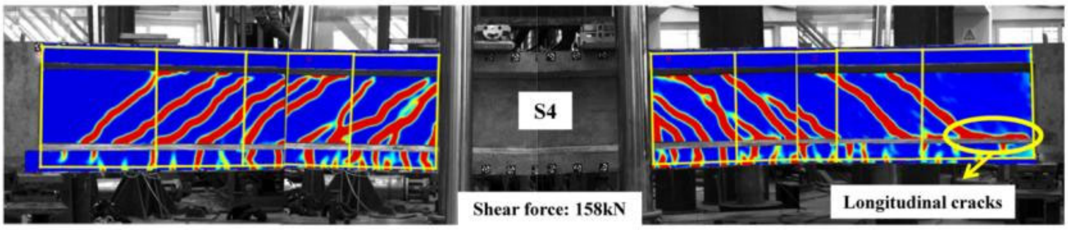

Fig. 8 Crack patterns of S3 at the shear cracking loads of different virtual measuring grids

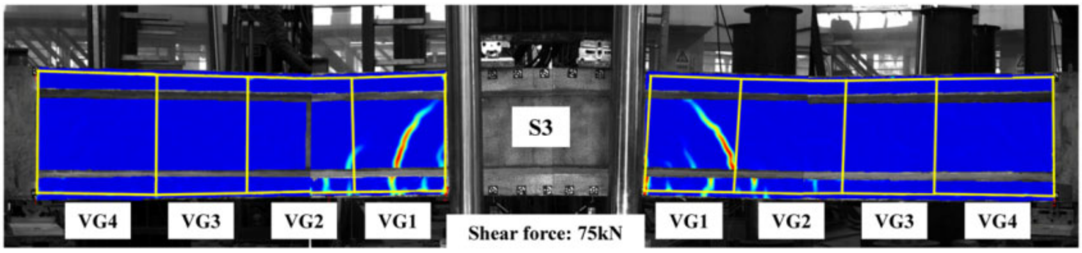

(a) Shear cracking of the left and right VG1

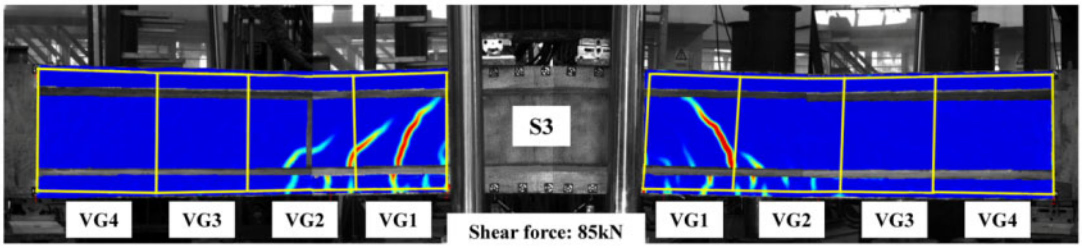

(b) Shear cracking of the left and right VG2

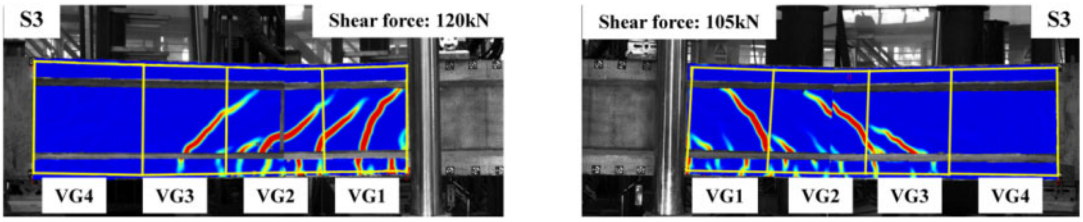

(c) Shear cracking of the left and right VG3

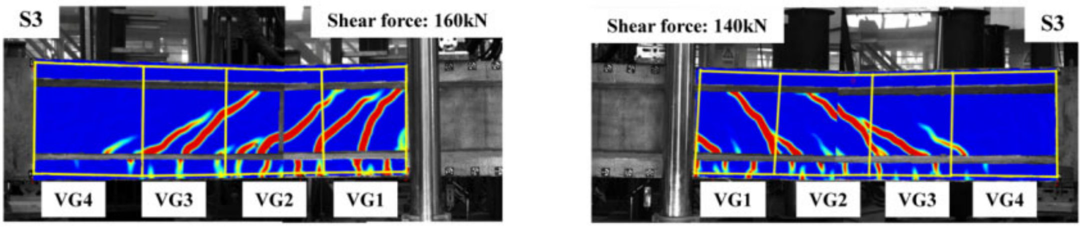

(d) Shear cracking of the left and right VG4

Fig. 9 Comparison of the experimental and calculated flexural cracking loads

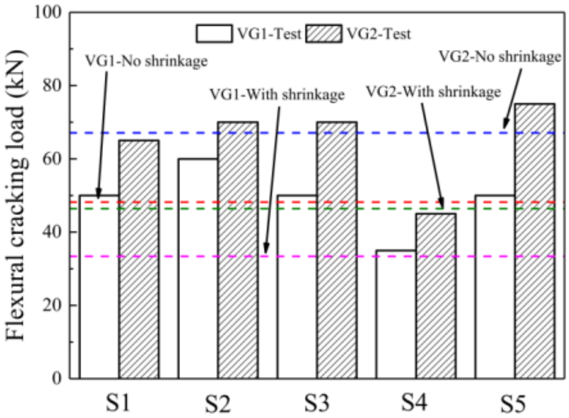

Fig. 10 Comparison of the experimental and calculated shear cracking loads

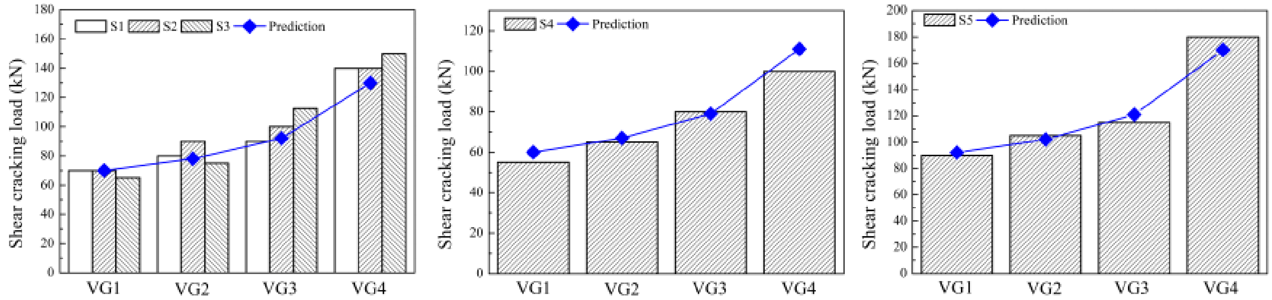

(a) S1, S2 and S3 (b) S4 (c) S5

963 **Fig. 11** Apparent yield strain of the steel reinforcement surrounded by concrete

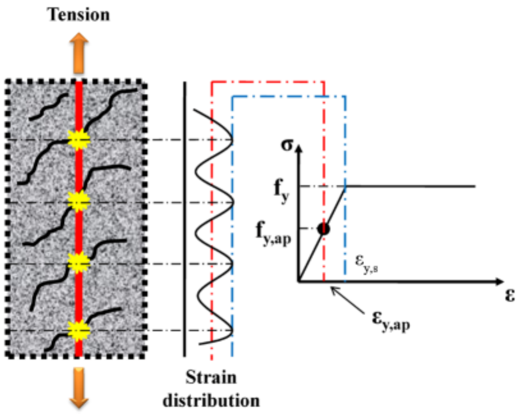

964

965

Fig. 12 Comparison of the experimental shear-induced deflections obtained by two different methods

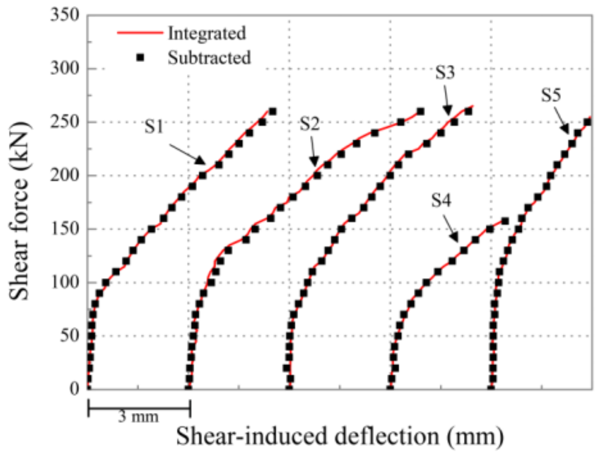

Fig. 13 Comparison of the experimental shear-induced deflections of the measuring zones in the left and right shear spans

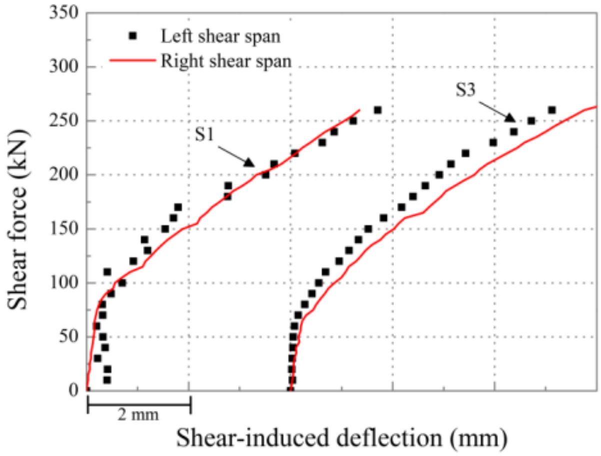

Fig. 14 Total deflections in the measuring zone

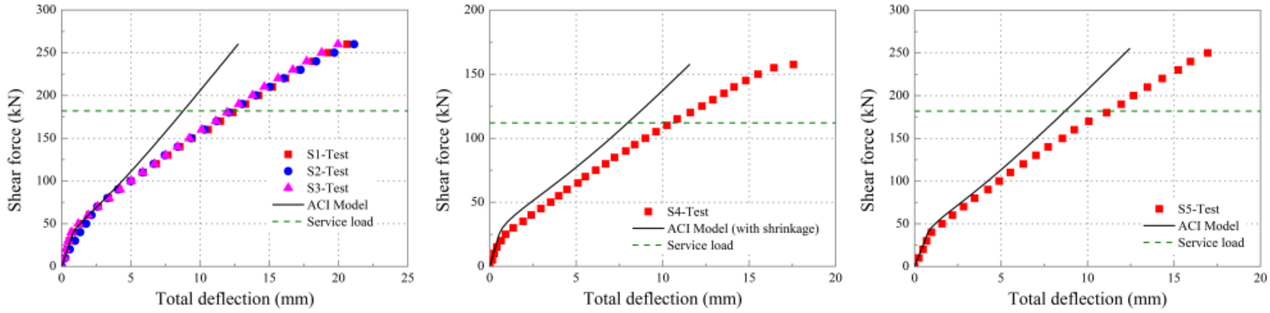

(a) S1, S2 and S3 (b) S4 (c) S5

Fig. 15 Experimental and predicted flexure-induced deflections in the measuring zone

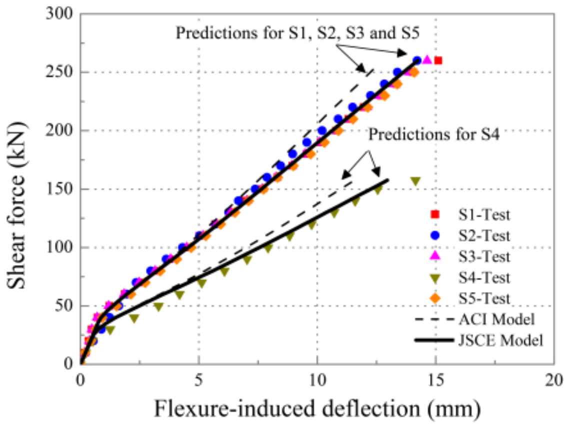

Fig. 16 Experimental shear-induced deflections in the measuring zone

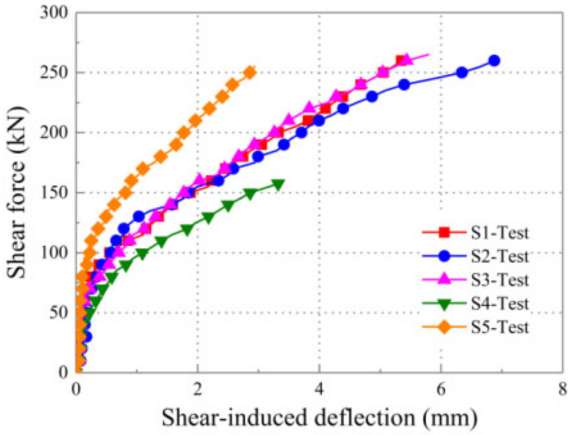

Fig. 17 Comparison of the measured and predicted shear-induced deflections

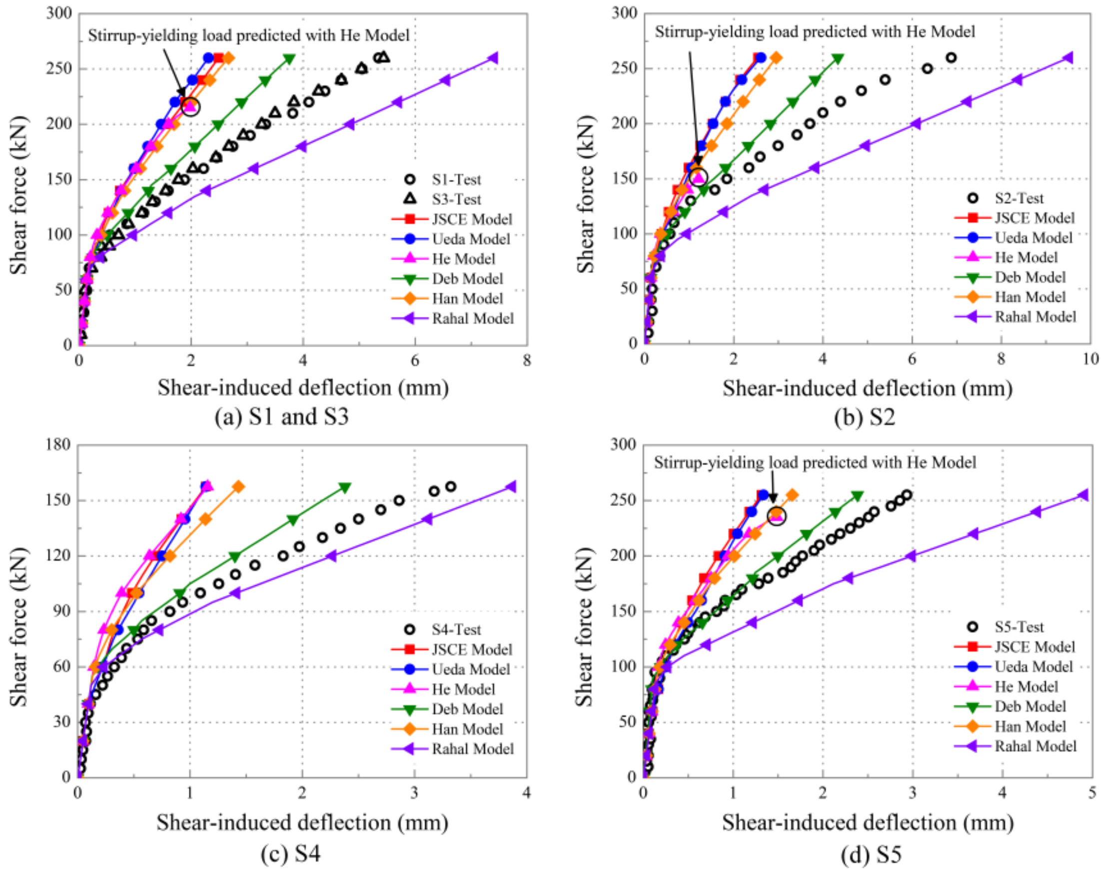

Fig. 18 Experimental mean shear strain of the grids with different moment-to-shear ratios of specimen S3

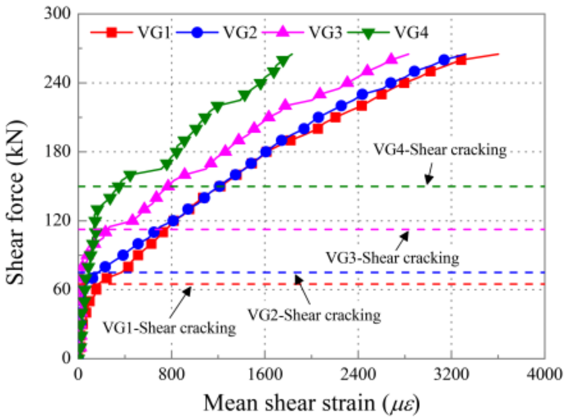

Fig. 19 Experimental principal compressive strain angles of the grids in S1

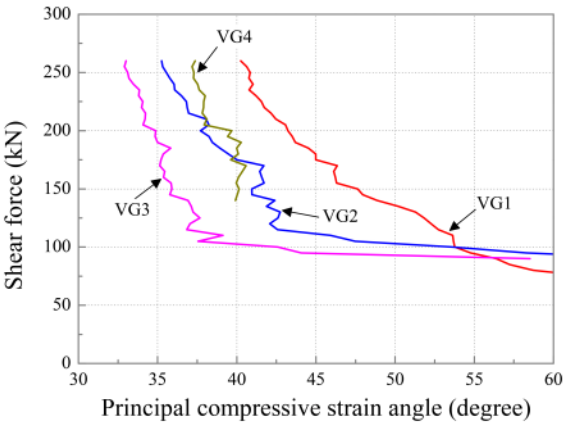

Fig. 20 Experimental principal compressive strain angles of VG2s in S1, S2 and S4

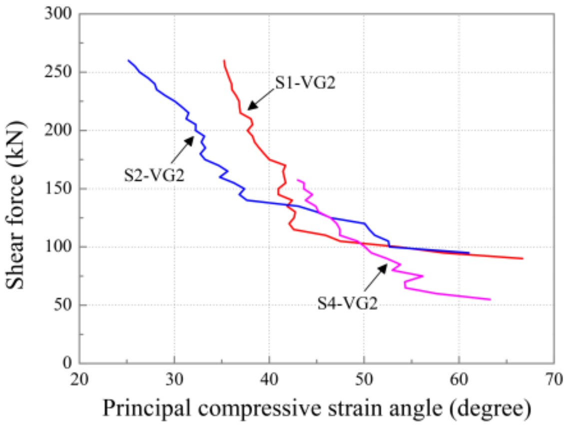

Fig. 21 Experimental and calculated principal compressive strain angles of the grids in S1

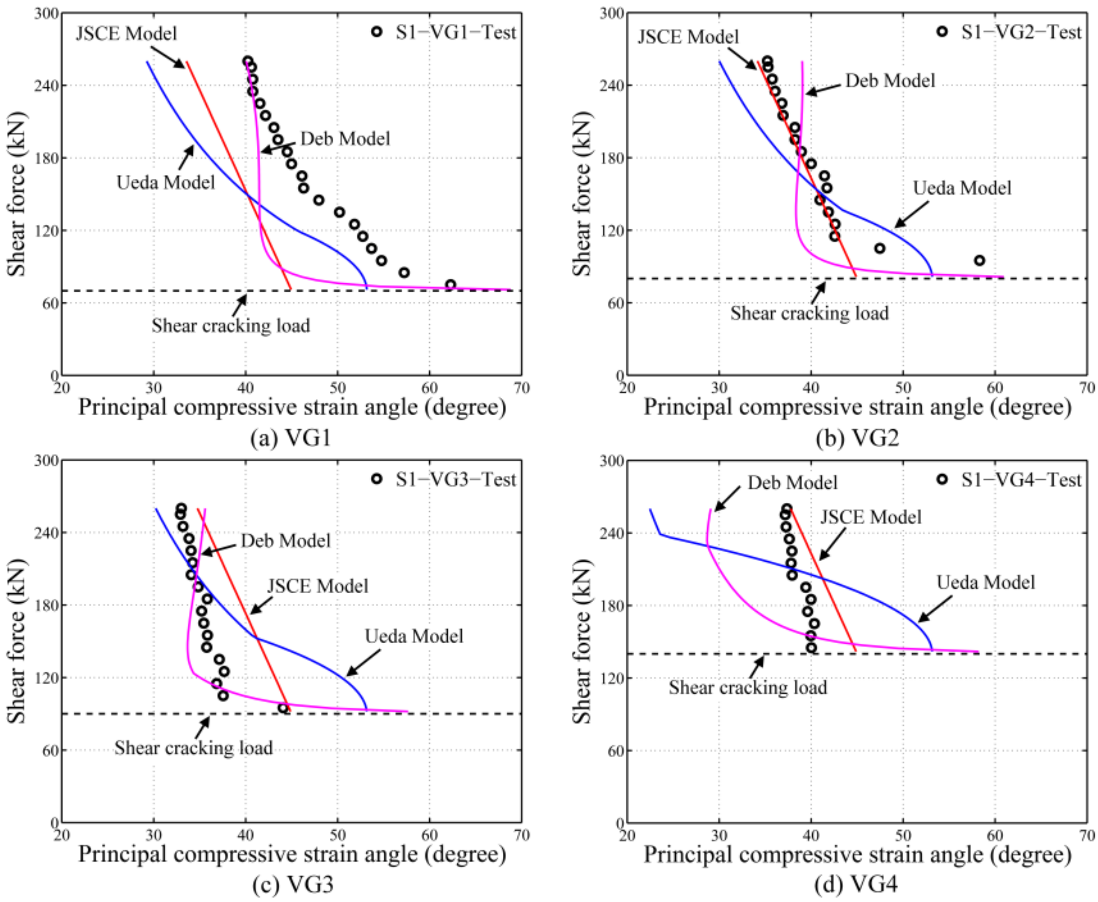

1000 **Fig. 22** Principal compressive strain of the grids in S3

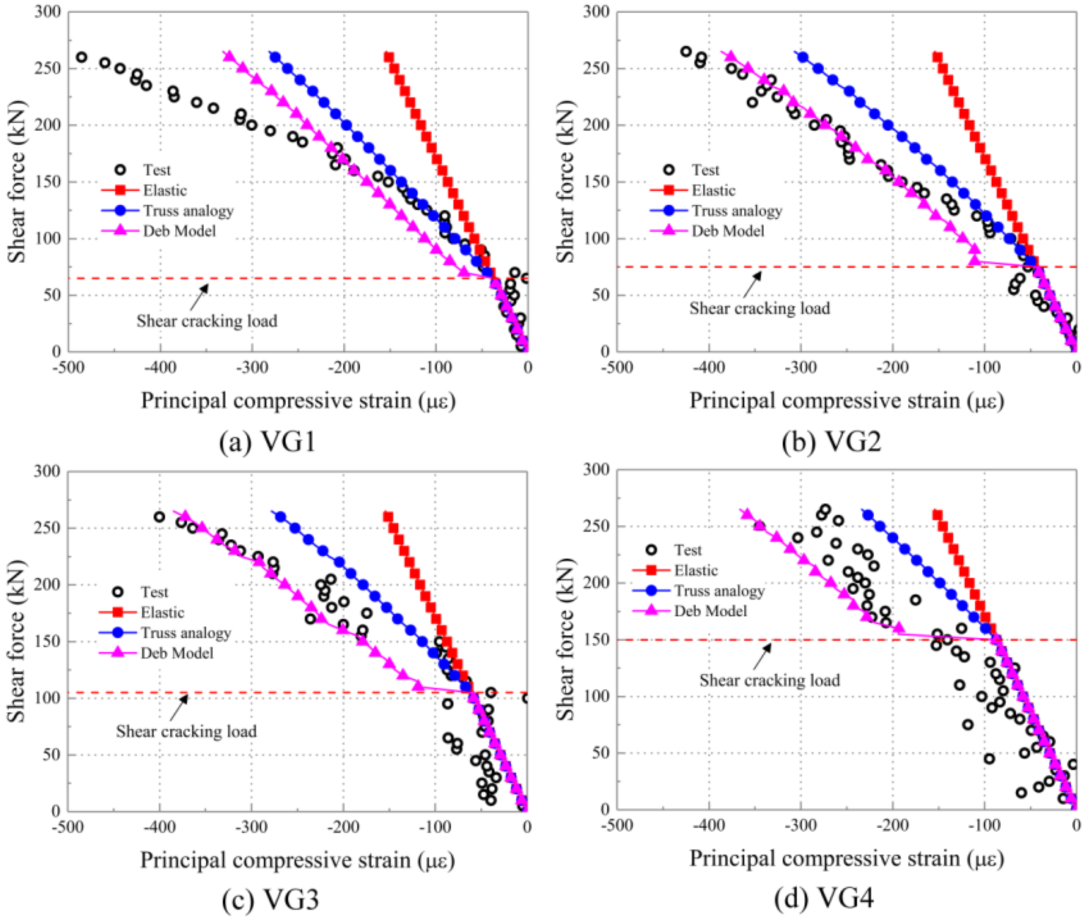

1001

Fig. 23 Experimental and calculated mid-depth longitudinal strain of VG3s in S1

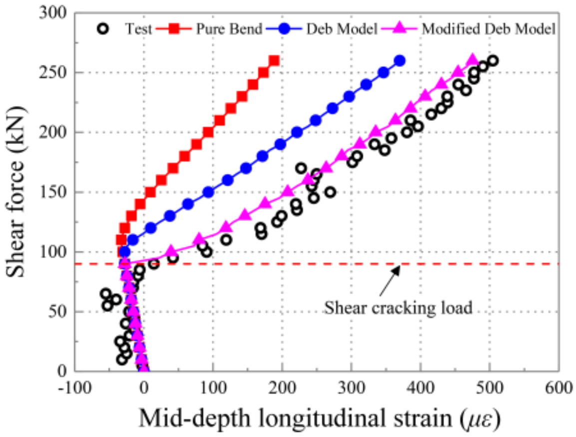

Fig. 24 Calculated shear-induced deflections with the preliminary "Modified" Deb Model

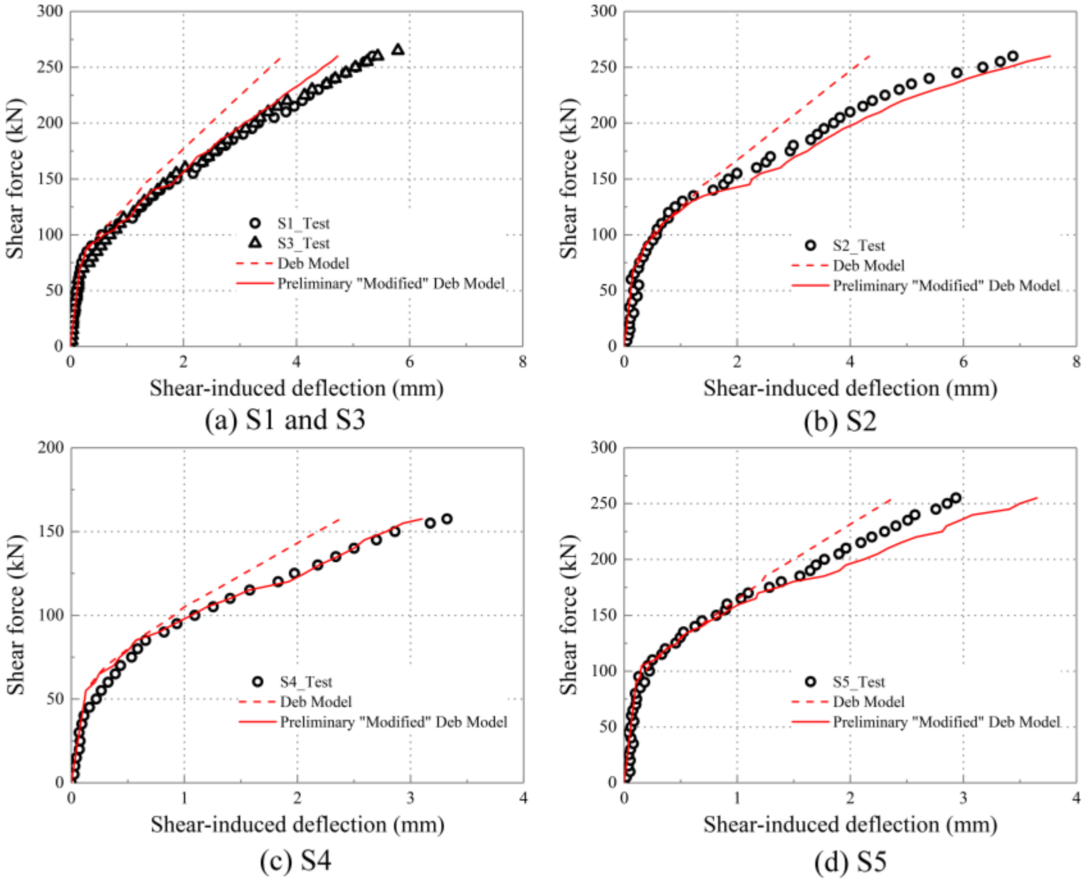

Fig. 25 Experimental and calculated mean vertical strain of the grids in S1

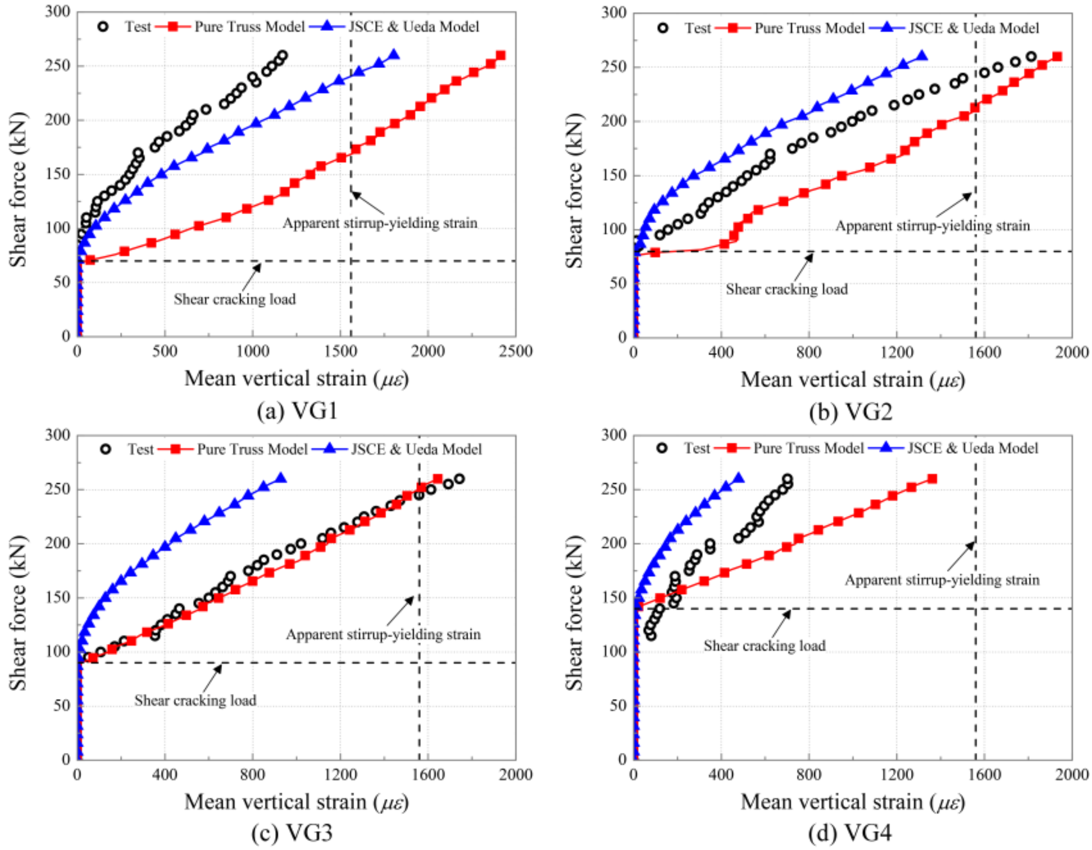

Fig. A1 Experimental and calculated mean vertical strain of the grids in S2

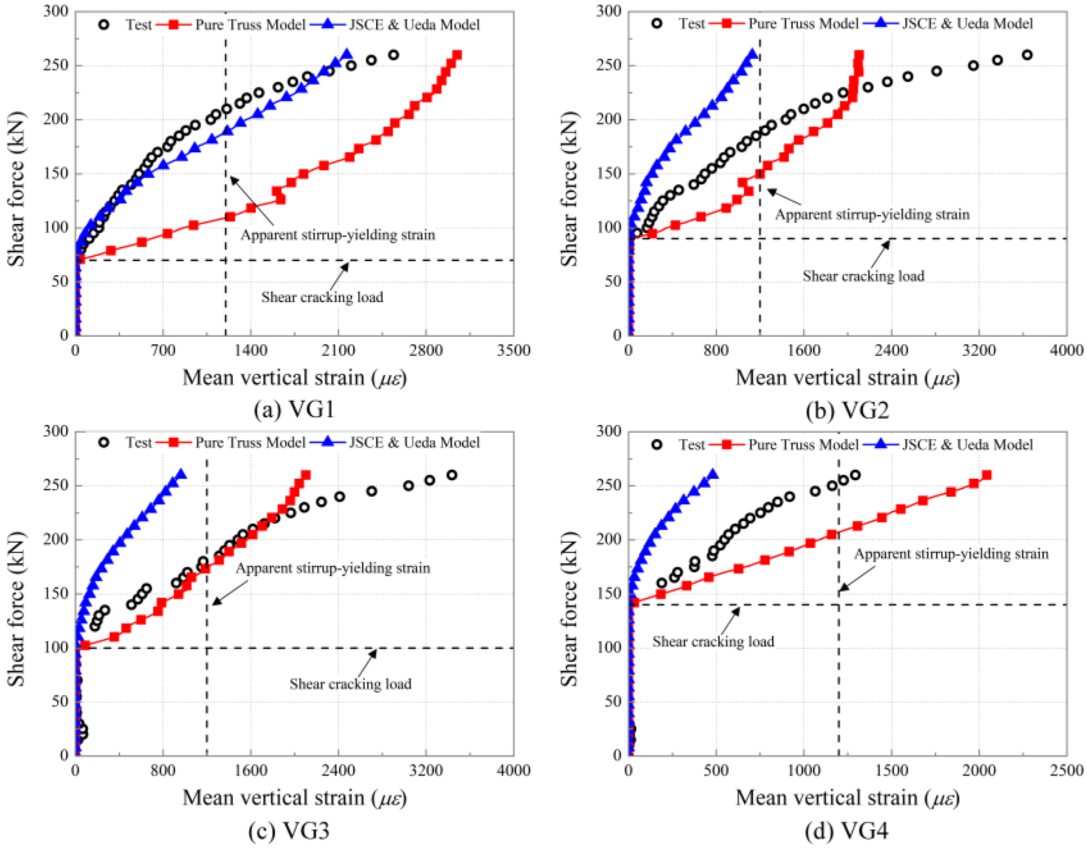

(a) VG1 (b) VG2 (c) VG3 (d) VG4

Fig. A2 Experimental and calculated mean vertical strain of the grids in S3

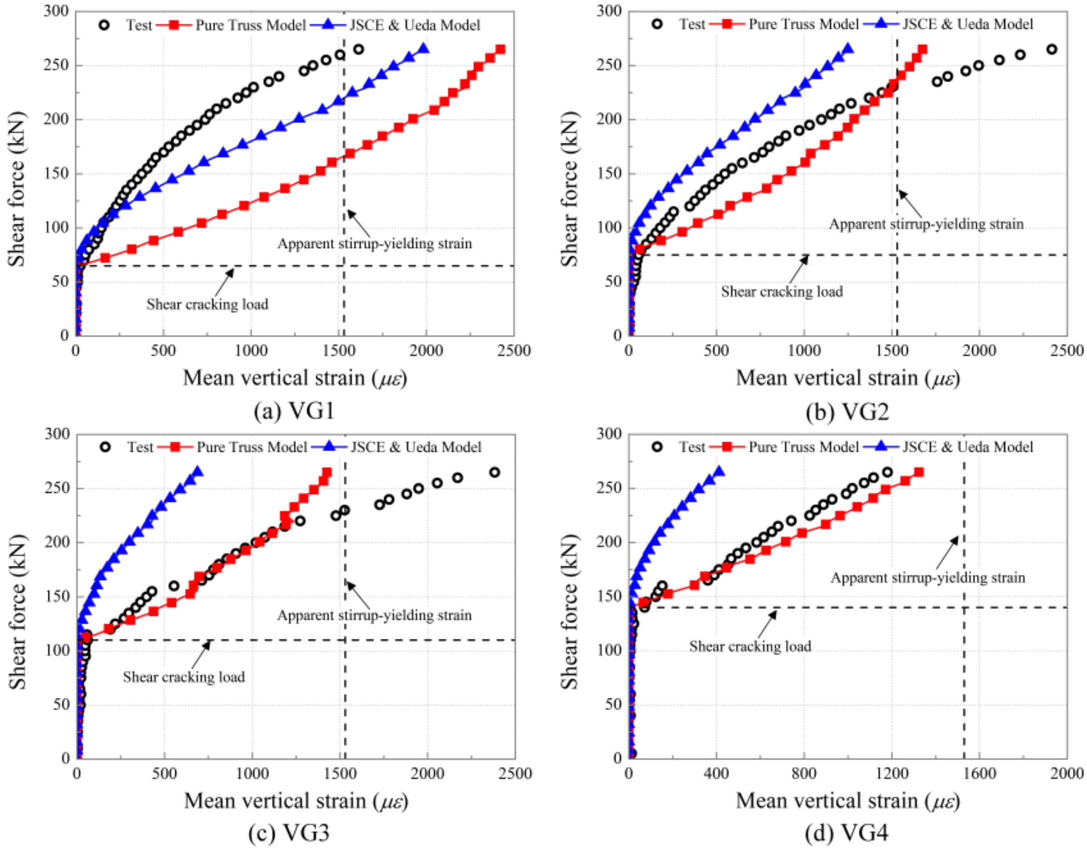

Fig. A3 Experimental and calculated mean vertical strain of the grids in S4

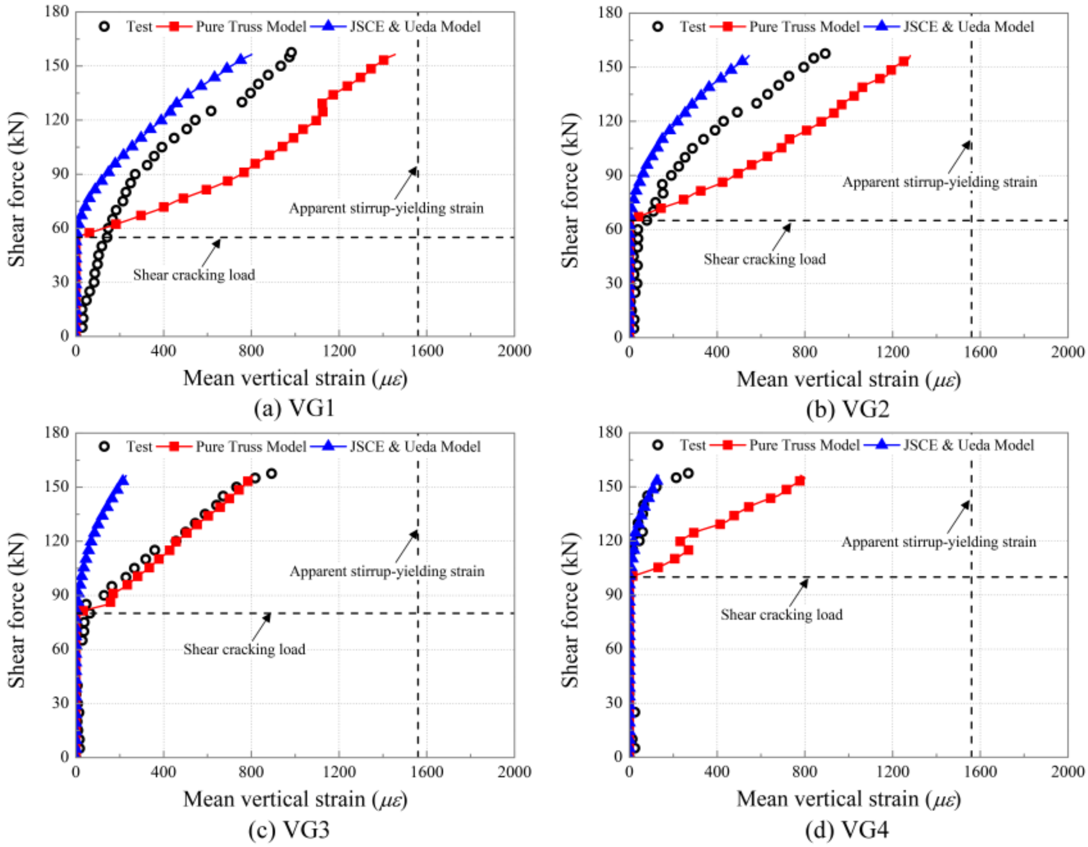

Fig. A4 Experimental and calculated mean vertical strain of the grids in S5

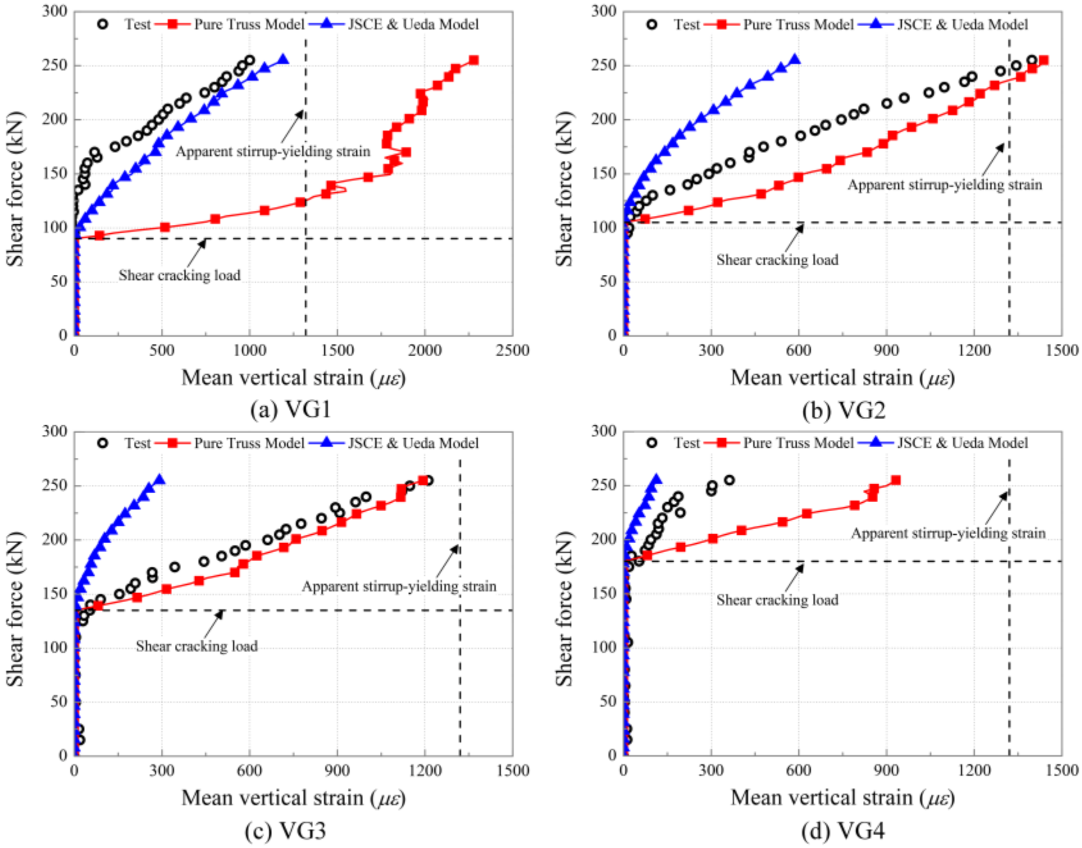

Fig. A5 Experimental mean shear strain of the grids of all specimens in this paper

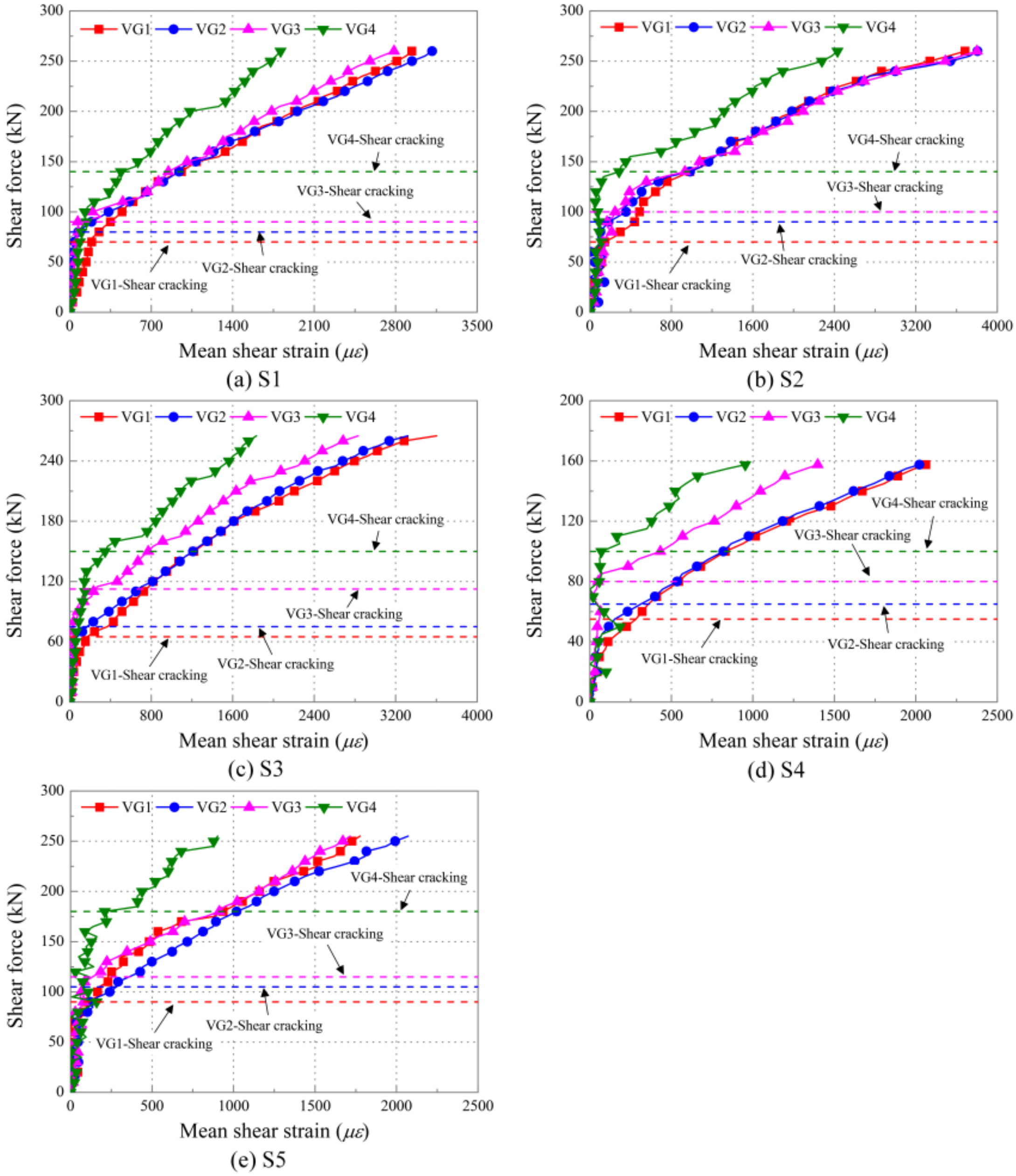

Fig. A6 Experimental and calculated principal compressive strain angles of the grids in S2

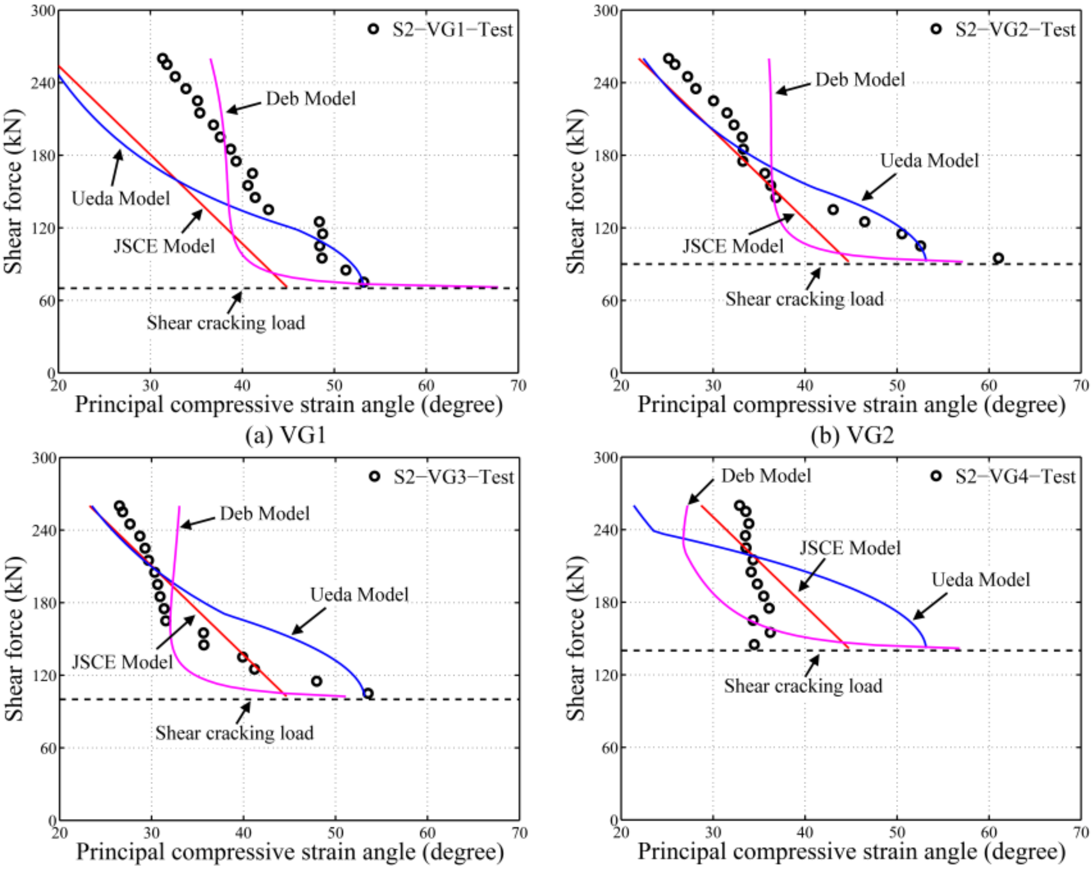

(a) VG1 (b) VG2 (c) VG3 (d) VG4

1032 **Fig. A7** Experimental and calculated principal compressive strain angles of the grids in

1033 S3

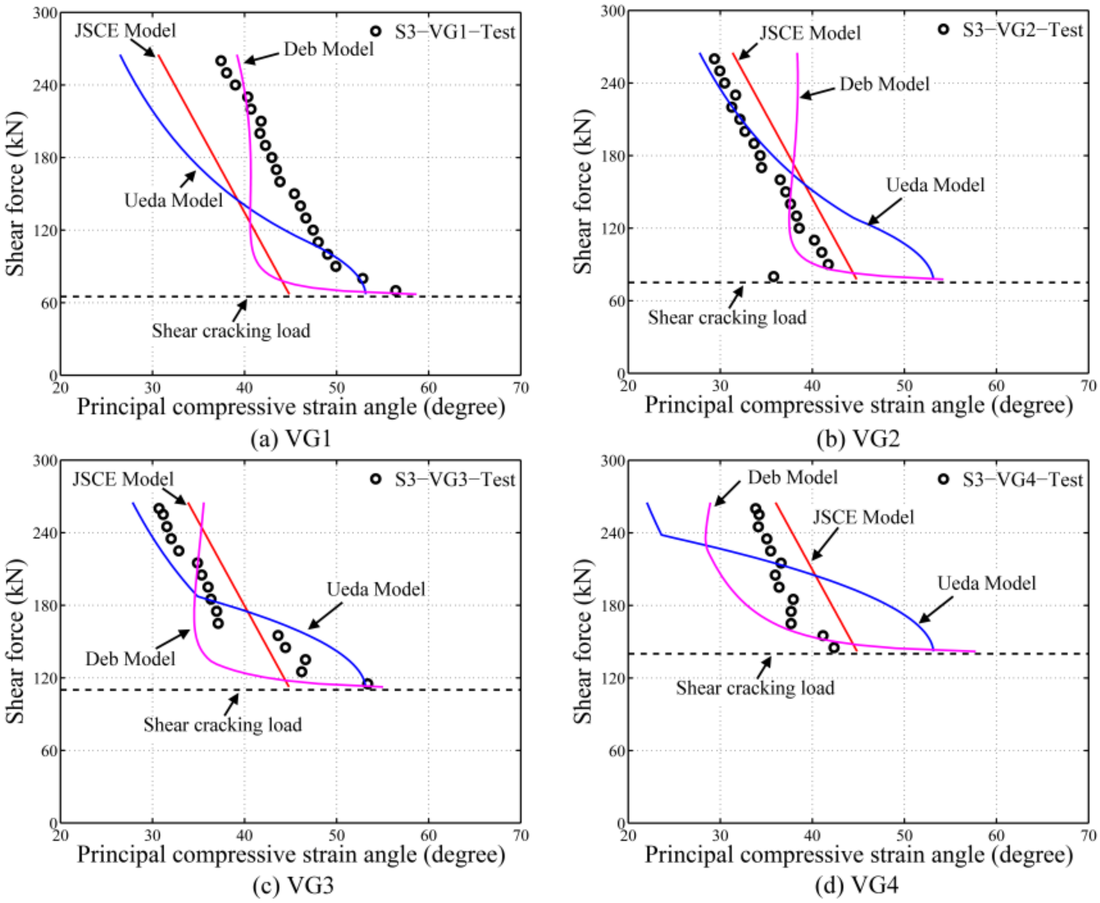

1034

1035

Fig. A8 Experimental and calculated principal compressive strain angles of the grids in S4

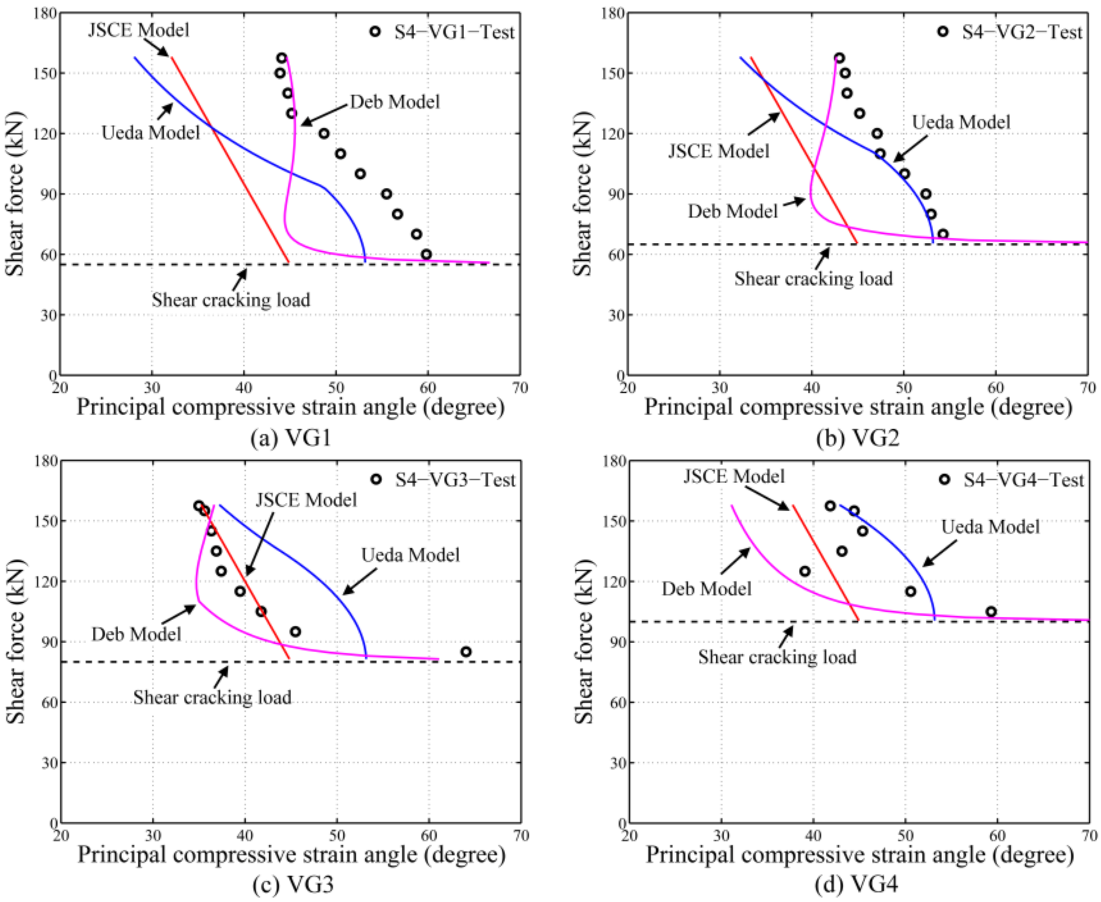

Fig. A9 Experimental and calculated principal compressive strain angles of the grids in S5

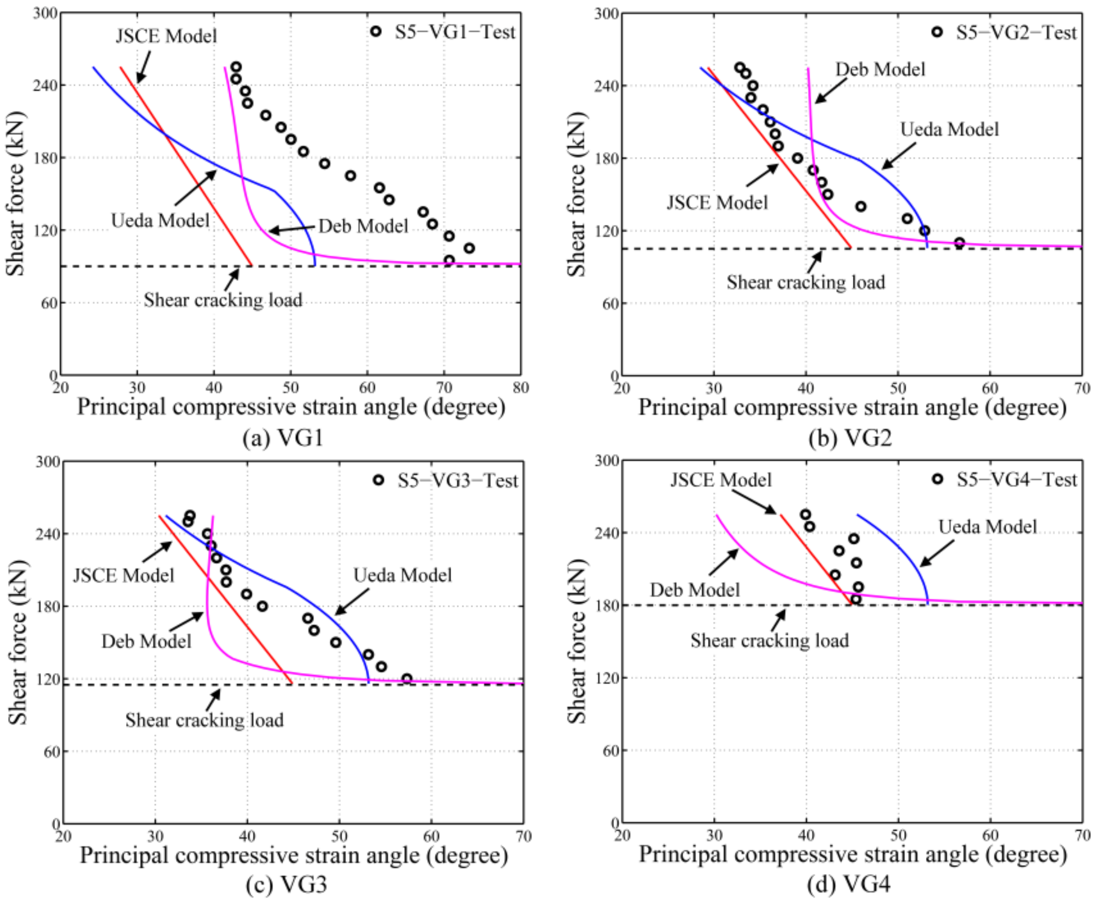

Fig. A10 Experimental and calculated mid-depth longitudinal strain of VG3s in specimen S2 to S5